



universität
wien

MASTERARBEIT

Titel der Masterarbeit

Seismogenic-triggered soft sediment deformation (Hirlatzhöhle, Austria)

verfasst von

Martina Lan Salomon, BSc

angestrebter akademischer Grad

Master of Science (MSc)

Wien, 2015

Studienkennzahl lt. Studienblatt:

A 066 815

Studienrichtung lt. Studienblatt:

Masterstudium Erdwissenschaften

Betreut von:

Univ.-Prof. Mag. Dr. Bernhard Grasemann

Seismogenic-triggered soft-sediment deformation

(Hirlatzhöhle, Austria)

Für Papa

CONTENTS

1. INTRODUCTION	6
2. STUDY SITE	7
2.1 Geographical setting	7
2.2 The Hirlatz Cave	7
2.2.1 Discovery and History of the Hirlatz Cave	7
2.2.2 Geological setting	8
3. SPELEOSEISMOLOGY	12
4. METHODOLOGY	15
4.1 Outcrop Analysis	15
4.2 X-ray diffraction (XRD)	15
4.3 Heavy mineral analysis	16
4.4 Structural analysis	17
5. RESULTS	19
5.1 Sedimentological observations	19
5.1.1 Bulk composition under the XRD	19
5.1.2 Clay mineral analysis (<2 µm fraction)	20
5.1.3 Heavy Mineral analysis	21
5.2 Structural analysis	21
5.2.1 Current ripples	22
5.2.2 Water escape structures	22
5.2.3 Syn-slumping faults and folds	23
5.2.4 Domino-Boudins	27
6. DISCUSSION	35
6.1 Potential source of seismic events	35
6.2 Interpretation of sedimentological investigations	36
6.3 Estimation of periodicity	38
6.4 Structural interpretation	38
7. CONCLUSION	40
8. ACKNOWLEDGMENT	42

Appendix

51

A. APPENDIX	52
-------------	----

ABSTRACT

The present study focuses on deformed cave sediments, that have been well protected from both the erosional processes occurring at the earth's surface and anthropogenic activities. Therefore they provide an unique archive to record paleo-seismicity, as well as an opportunity to assess potential regional seismic hazards.

The study focuses on a 6.8 m long x 3 m high outcrop wall within the Hirlatzhöhle (Upper Austria). Sedimentological investigations under the XRD of the unconsolidated finely laminated clay-sized sediments show varve-like layering of brighter carbonate and quartz rich layers, and darker clay mineral rich layers. Furthermore heavy mineral analysis have been undertaken, to estimate the origin of the source rock. Within this fine laminated layer-cake, even the smallest effect of deformation can be recorded and numerous soft sediment deformation structures are preserved. The succession contains abundant millimeter to centimeter-scale seismogenically induced flame and frishtail structures, domino boudins and syn-slumping structures such as folds and fault (normal and thrust faults) with flanking structures.

Geometric analogues has been described 2-3 orders of magnitudes larger (e.g. Alsop et. al, 2011) close to the Dead Sea Fault. Quantitative techniques, such as the reconstruction of the aspect ratios of boudins, the fault system polarity, the coefficient of variation of faults and kinematic balancing have been used to interpret the structures.

This leads us to the following conclusions that (i) the sediments where deposited under fluvio-lacustrine conditions and (ii) derive south from the Austroalpine Crystalline. Furthermore (iii) the the formation of the soft-sediment structures in the Hirlatz cave was triggered by cyclic seismic events, (iv) the structures were mainly formed in the uppermost, highly water saturated layers, and (v) liquefaction resulted in density discontinuity, decreasing the shear strength within the stratified layers. Minor seismicity recorded along the Salzach-Ennstal-Mariazeller-Puchberger (SEMP) sinistral strike-slip fault, which has a maximum displacement of > 60 km, prove recent seismic activity. This lies about 15 km south of the outcrop, accommodates the active extrusion of the Eastern Alps towards the Pannonian Basin and is a possible source for the cyclic seismic events within the Hirlatz cave.

ZUSAMMENFASSUNG

Die vorliegende Arbeit beschäftigt sich mit Höhlensedimenten. Gut geschützt vor Erosionsprozessen und anthropogenen Einflüssen an der Erdoberfläche stellen diese Sedimente ein einmaliges Archiv für Paleoerdbeben dar und helfen uns mögliche regionale seismische Gefahren zu verstehen und abzuschätzen.

Die Untersuchungen der Arbeit konzentrieren sich auf einen 6.8 m langen x 3 m hohen Aufschluss in der Hirlatzhöhle (Oberösterreich). Sedimentologische Untersuchungen wie beispielsweise die Röntgendiffraktometrie, welche an fein laminierten Sedimenten durchgeführt wurde, weisen eine warvenähnliche Struktur von helleren, Karbonat- und Quarz-reichen und dunkleren tonmineralangereicherten Lagen auf. Um die Herkunft des Ursprungsgesteins zu bestimmen wurden an den unkonsolidierten Ablagerungen, Schwermineralanalysen durchgeführt.

Detaillierte Beobachtungen der einzelnen Lagen zeigen, mm- cm große erdbebeninduzierte Strukturen, wie zum Beispiel Flammen und Fischflossen ähnliche Strukturen, Boudins mit Dominogeometrie und syn-Rutschungsstrukturen wie Falten und Störungen (normal and thrust faults). Vergleichbare Strukturen sind 2-3 Ordnungen größer als dem Totem Meer bekannt (z.B. Alsop et.al., 2011). Quantitative Methoden, wie die Rekonstruktion der Seitenverhältnisse einzelner Boudins, die Polarität und der Variationskoeffizient der Störungssysteme, sowie das Bilanzieren der kinematischen Abläufe wurden angewendet, um die Strukturen zu interpretieren.

Dies führt zur Annahme, dass (i) die Sedimente unter fluvio-lakustrinen Bedingungen abgelagert wurden, und (ii) aus dem südlich angrenzenden Kristallin stammt. Die untersuchten Strukturen zeigen, dass sie (iii) durch zyklische seismogene Aktivität induziert wurden (iv) hauptsächlich an der wassergesättigten Sedimentoberfläche im Kontakt zum Wasser gebildet wurden (v) und dass die Liquefizierung und Dichteunterschiede der einzelnen abgelagerten Schichten zu einer Senkung des Scherwiderstandes führt. Geringe seismische Aktivitäten sind von der Salzach-Ennstal-Mariazeller-Puchberger-Störung (SEMP) bekannt. Die sinistrale Seitenverschiebung weist einen maximalen Versatz von > 60 km auf und befindet sich etwa 15 km südlich der Hirlatzhöhle. Weiters findet entlang der SEMP die aktive Extrusion der Ostalpen gegen das Pannonische Becken statt. Die Störung könnte eine mögliche Quelle für die zyklischen seismischen Events in der Hirlatzhöhle sein.

INTRODUCTION

Caves play an important role for paleo and neotectonic studies and to record the minor deformation rates. In Austria there are only little evidences of younger active tectonics, especially in the Alps, which have been affected by a high erosion rate during the Quaternary glaciations, therefore caves provide an perfect study site. Traces of seismogenic activity in caves can be observed in:

- Speloethemes: broken and tilted stalagmites, growth anomalies, displacement of stalactite-stalagmite pairs, fallen stalactites (e.g. Becker et al. 2012, Becker et al 2006, Plan et al. 2010)
- Incasion: Incasion means a single rockfall or the collaps of a cave section (e.g. Becker et al., 2006)
- Sediment deformation (e.g Lingier & Desmet,2002)

In the Eastern Alps only one known study, deals with neotectonics in caves (Plan et al., 2010). In this work the first evidence of neotectonic evidence in the Eastern Alps was dated with the U/Th method on spelothemes. Flowstone damages and passage dislocation were observed in the Hirschgruben cave, which lies along the SEMP. The deformed cave features were there created by one or more tectonic events and dated to the last glacial period or the earliest part of the Holocene. (Plan et al.,2010).

Ambition of the recent study on soft sediment deformation within the Hirlatz cave, is

- to fill a gap in the record of paleoearthquakes
- estimate the occurence of seismic activity in that particular region
- to document seimogenic induced sturctures in soft sediments
- understand potential futrure regional hazards

STUDY SITE

2.1 GEOGRAPHICAL SETTING

The Hirlatz Cave (870 m ASL, Number of Austrian Cave Register: 1546/7) lies in the Northern Calcareous Alps (NCA) about 2 km SW of the UNESCO world heritage Hallstatt (Upper Austria). The cave entrance is located in the Echerntal on an approximately 900 m vertical north face of the Hirlatz in an altitude of 870 m ASL. (Buchegger & Greger, 1998) The cave is situated the SW part of the Dachsteinplatteau, a Triassic carbonate platform in the tectonic unit of the Dachstein nappe, which mainly consists of Dachsteinkalk (Buchegger & Greger, 1998) With a length of 101 km and a depth of 1070 m this karstic cave is the third largest known cave system in Austria, only the Schönberg cave system with a length of 140 km in the Totes Gebirge is longer (Pfarr *et al.*, 2014). Focus of the present study is on a 6.8 x 3 m vertical outcrop wall, that lies within the Hirlatz Cave in the so called Lehmklamm located about 2.8 km SE of the cave entrance.

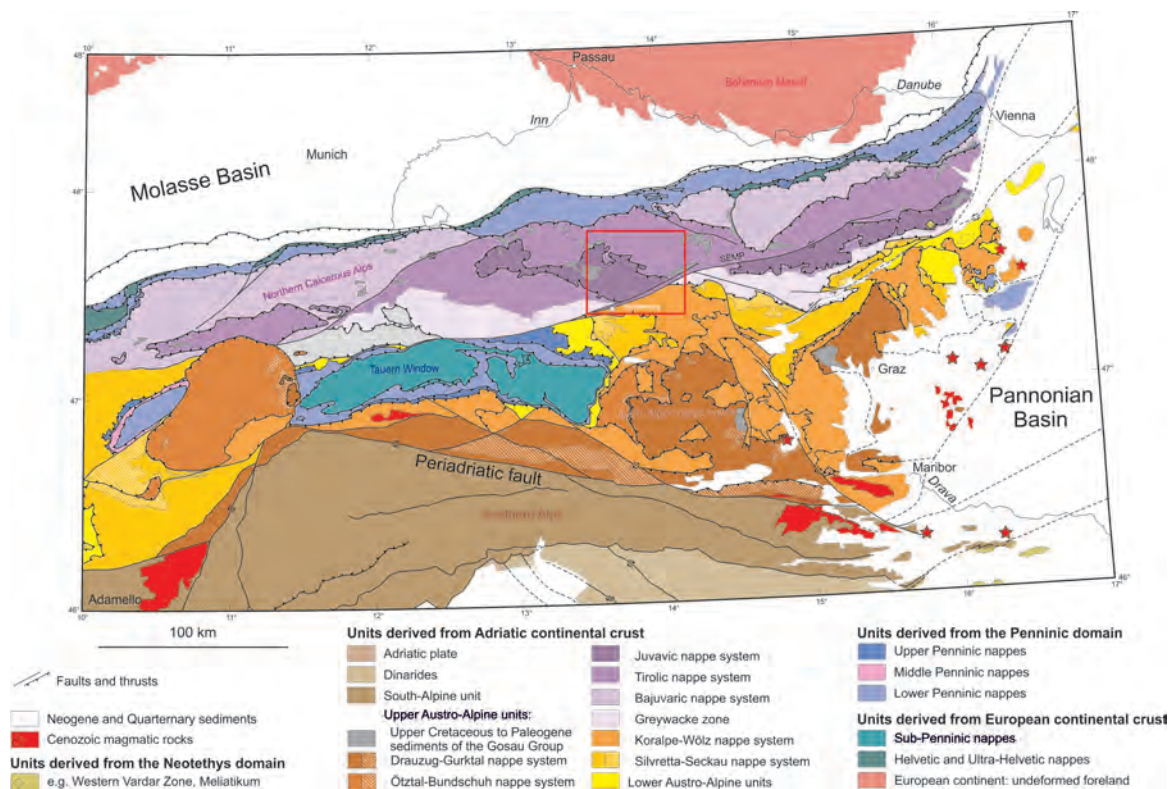


Fig. 1: Tectonic map of the Alps, Schuster *et al.* (2010) after Schmid *et al.* (2004).

2.2 THE HIRLATZ CAVE

2.2.1 Discovery and History of the Hirlatz Cave

The first try to reach the Hirlatz cave was made in 1924 by Georg Lackner and his brother Fritz, who failed on the 7 m vertical wall below the cave entrance. Long time before people were considering systematical karsthydrological investigations and speleology, the karst plateau and the karst springs were of interest. Some evidence that support the latter were found: (i) a neolithic stone axe, that has been found near Kessel, a karstic spring and (ii) the existence of an adit at the Hirschbrunn, which must be older than 1573 (Buchegger & Greger, 1998). In 1927 Johann Höll, Matthias Kirchschalger and Karl Mitterhauser started a new attempt to get into the cave

and carried up a tree from the valley to climb up the steep wall to reach the cave entrance. They managed to get 30 m deep into the Hirlatzcave, until they reached a sump. After World War II in 1949, five young men did the next attempt to climb into the cave, they also had to stop at the sump, like their colleagues before in 1924. On November 26th, 1949 Gerog Lackner (son of Gerog Lackner, who tried to get into the cave 1924), Karl Pilz and Franz Vockenhuber got about 250 m, till the Lehmhalle which was later renamed to Karl-Pilz-Halle. This day is assumed to be the discovery day of the Hirlatzhöhle (Buchegger & Greger, 1998). Until today numerous expeditions and a lot of detailed work has been done to explore the approximately 101 km long cave system. The cave extends from the entrance at the north face of the Hirlatz into southern direction below the Wiesberghaus. In the west it reaches till the Grünkogel and in the east it extends underneath the Rauherkogel nearly until the Kessel (Pohl & Greger, 2001).

2.2.2 Geological setting

The Northern Calcareous Alps (NCA) are the uppermost tectonic unit in the Eastern Alps and form a 500 km long and 20 to 50 km wide thrust belt. The sedimentary deposits represent the tectonosedimentary history of the Eastern Alpine part of Tethyan shelf from Permian to Eocene times. In Permian the deposition on the Variscan metasedimentary basement starts with continental to shallow marine siliciclastics and evaporites. (Mandl, 2000) At the end of Early Triassic carbonate production starts to dominate the stratigraphic succession and continues in Middle to Late Triassic, characterized by carbonate platforms. The Dachstein nappe represents a distal shallow marine shelf of the Tethys, neighbored by pelagic limestones of the deeper shelf, the so-called Hallstatt facies, where Permian synsedimentary evaporite diapirism can be found. The transitional depositions from Hallstatt facies to radiolarites, representing oceanic conditions, are not preserved in the NCA. The Dachstein nappe, the tectonic unit in which the Hirlatz cave has developed, represents a distal shallow marine shelf of the Tethys. (Mandl, 2000)

Presently the most common assumption is that the NCA was a passive continental margin during Permo-Triassic times which was bordered by the "Hallstatt-Meliata-Ocean" (Kozur, 1991) and has been closed during Jurassic times. During opening of the Penninic ocean in the early Jurassic, the Austroalpine including the NCA has been detached from the European plate. Transpression of the Tethys margin accompanied by penninic rifting and resulted in the first displacement of Juvavic nappe system and basin successions into the Tyrolic basins. During Late Jurassic to Paleogen, in the course of Alpine orogeny and during several stages of deformation a complex nappe system was created. The Mesozoic sediments were partly detached from the Variscan basement into northern direction, mainly along facies boundaries. Nowadays the allochthonous sediments are found as tectonic bodies on top of the Rhenodanubian Flysch Zone in the north and in contact with the Variscan basement (Greywacke Zone, Noric nappes) in the south. From north to south, and from bottom to top the NCA consists of the Bajuvaric nappe complex, Tyrolic nappes and the Juvavic nappe system representing the uppermost tectonic unit. (Mandl, 2000)

After a period of erosion on top of the nappe stack Late Cretaceous clastic sediments of the Gosau Group were deposited. Strike slip movements e.g. SEMP (Salzach-Ennstal-Mariazeller-Puchberger) fault system have accompanied the Miocene uplift of the Eastern Alps and also affected the NCA (Mandl, 2000) and activated a diagonal joint system in NW-SE- and NE-SW-direction. The resulted joints are refilled by Hirlatzlime (Buchegger & Greger, 1998).

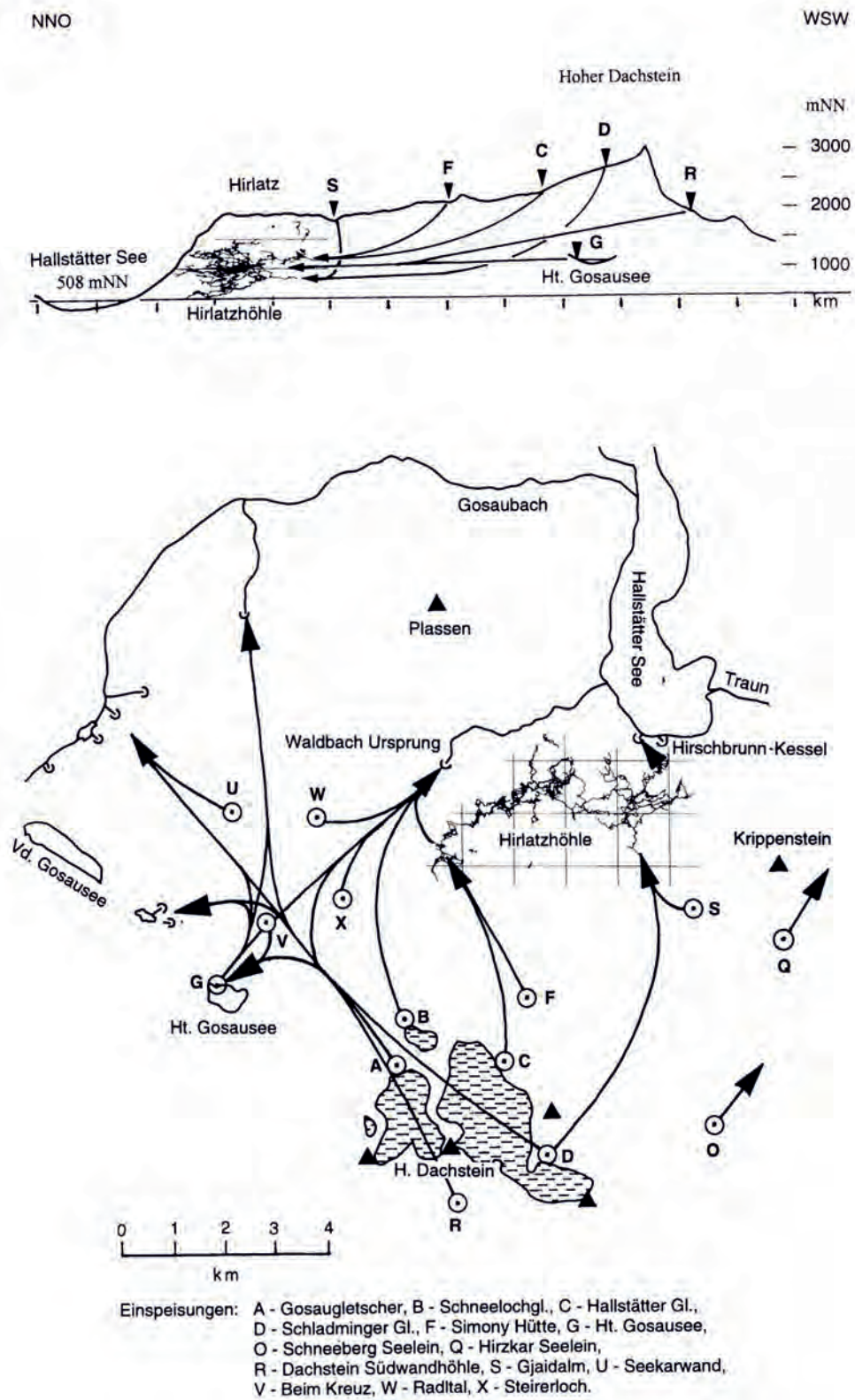


Fig. 2: Tracing paths in the western part of the Dachsteinmassif Pohl & Greger (2001).

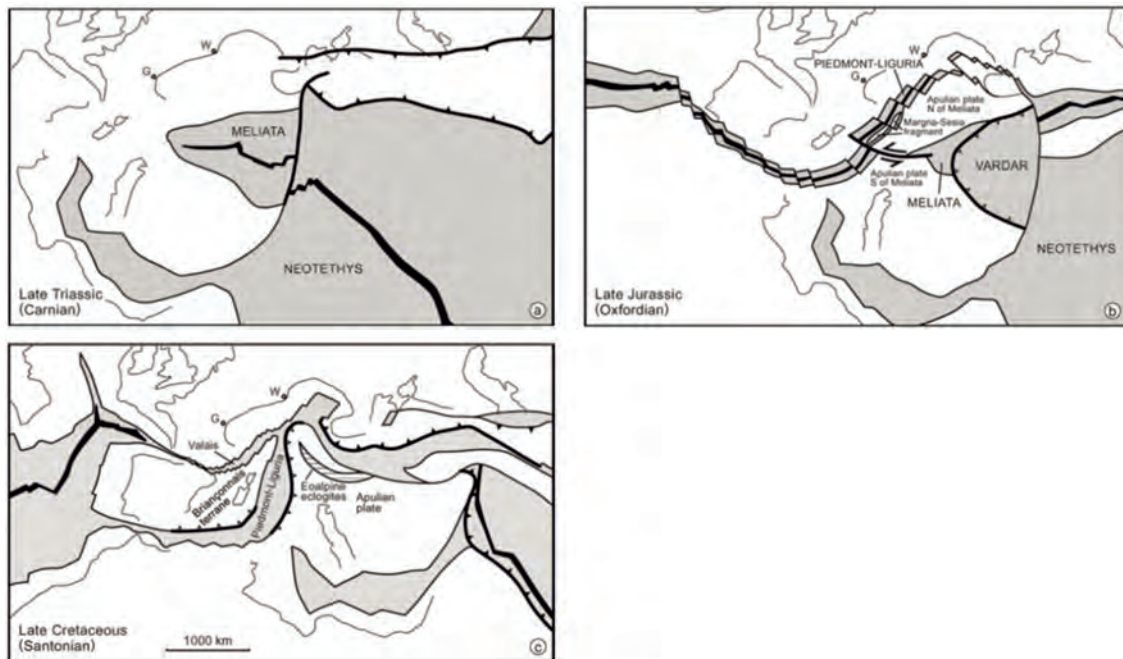


Fig. 3: Large-scale paleogeographic reconstruction for (a) Late Triassic, (b) Late Jurassic and (c) Late Cretaceous times. G: Genève; W:Wien Schmid *et al.* (2004).

The evolution of karstic caves depends on of effective water paths within the karstifiable rock and on the sedimentary bedding. Requirements to form a cave are all fulfilled in the Dachstein area. In the area around the Hirlatz Cave we find up to over 1.5 km thick sequences of Dachsteinkalk mainly north- directed dipping and dolomitic layers in-between, along which the water paths follow.(Buegger & Greger, 1998)

Dachsteinkalk describes ab litho-stratigraphic sequence which was deposited during Triassic times (245-204 Mio a.b.p) Buegger & Greger (1998) (Fig.4). It is characterised by bedded to massive light grey limestones. The more common bedded Dachsteinkalk, was deposited in sheltered lagoons and show sedimentary cycles, the so called Lofer-Zyklothem⁵. During deposition parts of the carbonate plattform were periodically dried up (Horizon A, reworked horizon). In the following step alga laminae developed in the intertidal to subtidal zone (Horizon B). In Horizon C within the subtidal zone Megalodon bearing limestones were deposited.Faupl (2003)

J U R	Malm < 5 m	Radiolarit (locally)
	Dogger	Dachsteinkalk- Breccia (locally)
	Lias	red Hirlatzlime and joint filling (remanent)
T R I A S	Rhaetian < 1500 m	bedded Daksteinkalk
	Norian < 200 - 500 m	Hauptdolomit and locally dolomitic Dachsteinkalk
	Carnian 0 - 20 m	Lunzer Schichten
	Ladinian < 500 m	Wettersteindolomit
	Anisian	Guttensteiner Dolomite
	Skythian 0-200 m	Werfener Schichten, Sandstones, Schist
P E R M		Haselgebirge and Evaporites

Fig. 4: Stratigraphy of Dachstein-nappe after Buegger & Greger (1998).

Karsthydrological investigations from 1986 and 1990 show that flow from an injection point at the Simony Hütte (F in Fig. 2), and most probably from the Hallstätter Glacier (C in Fig. 2) run into the Hirlatz Cave via Grünkogelsiphon and from there to Waldbachursprung. An important investigation was made during tracing experiments at Schladminger glacier (D in Fig. 2) and at Gjaidalm (S in Fig. 2) tracers can be followed through the Donnerbachsystem within the Hirlatz Cave towards the Hirschbrunn and Kessel sources. Due to the geological setting the main drainage system flows towards the north. Observations done on other big cave systems in Ausria lead to the assumption, that in most cases the main galleries are inactive from a karsthydrological perspective. In the Hirlatz Cave not only the low lying galleries are water-bearing also in the higher levels epiphreatic conditions can be found. During flooding events epiphreatic canyons get flooded and act as a conduits. In the Alter Teil of the cave, phreatic conditions occur on an altitude up to 1000 m ASL and flows over canyons into the Obere Brandgrabenhöhle. Whereas in the western part phreatic conditions are found between 1100 m ASL and 880 m ASL, during flooding events water accumulates in the area of Dark Highway and flows into the Waldbach-Ursprung. If the backwater area is filled up it comes to an overflow. Those situation are therefore very dangerous within the Hirlatz Cave. (Bucheegger & Greger, 1998)

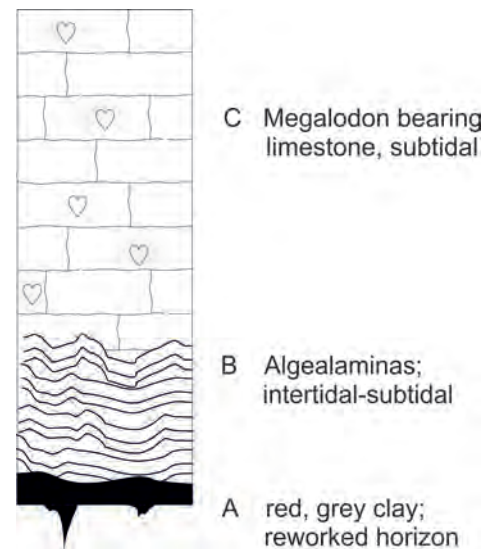


Fig. 5: Lofer Zyklthem, singel bed out of the Dachsteinkalk, cyclic sedimentation shows variation of the sealevel after Faupl (2003).

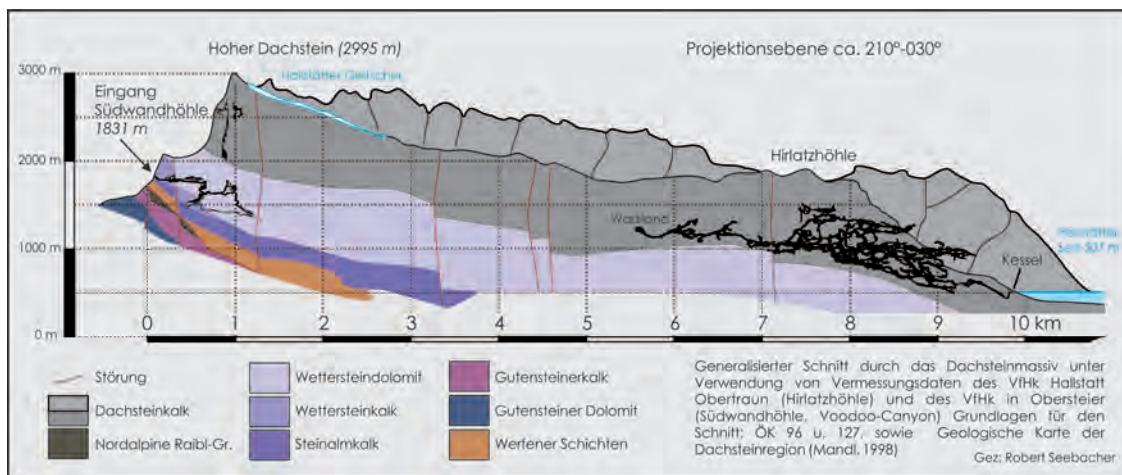


Fig. 6: Simplified cross-section through the Dachstein-massif based on ÖK 96 u. 127 and geological map of the Dachstein region Mandl (1998) drawn by Robert Seebacher (Seebacher, 2006).

Speleoseismology deals with earthquake records in caves (Becker *et al.*, 2006). Investigations of earthquake traces are found in speleothems (broken speleothems and growth anomalies), rockfall and displacement along bedding planes and faults and in sediment deformation (Becker *et al.*, 2006). Instrumental measurements of seismic activity started only by the end of the 19th century (Sandeep & Jain, 2007). Speleoseismology gives therefore important approaches to determine paleoearthquake activity and their reoccurrence in the past.

The investigated soft sediment deformation structures have been triggered by seismic shocks and are therefore known as seismites. To study seismic events, soft sediment deformation has proved to be especially useful. The term seismites has been introduced by Seilacher in 1969 (Seilacher, 1969). Seimite type structures have been also observed and described from many different areas in various tectonosedimentary environments such as in Pliocene deposits from the Prahova valley in Romania Brustur & Jipa (2007), in Pleistocene deposits around the Dead Sea Basin (Alsop & Marco, 2011, 2012a, 2013), in SE Spain (Rodríguez-Pascua *et al.*, 2000), in northern Brazil within the São Luís Basin (Rossetti, 1999), and in lake deposits in Turkey (Üner *et al.*, 2009). An Elderado to observe seismites can also be found in the Himalaya Sandeep & Jain (2007); Meyer *et al.* (2006); Draganits *et al.* (2014) Mohindra & Bagati (1996).

Conspicuous geometric analogies of 3-D sedimentary slump structures to the present study has been found next to the Dead Sea Basin in the Late Pleistocene, Lisan Formation Alsop & Marco (2011, 2012a,b, 2013). Studied fold and faults are dictated by very gentle slopes ($< 1\%$) and were seismogenic induced. The described contractional and extensional deformation structures in the Dead Sea Basin do show a wavelength of < 1 m and form packages less than 1 m up to 2 m and are 2-3 magnitudes larger, than the ones observed in the Hirlatz cave. The separation of the slumped units by horizontal strata leads to the assumption for being triggered by seismic events. Alsop & Marco (2011, 2012a,b, 2013)

Alsop categorized slump systems after hypothetical models in deformation cells. Interpretational models provide an useful framework to describe slump systems. Alsop & Marco (2011) Seismogenic induced shaking leads to an higher pore fluid pressure, the loss of cohesive strength within the cm- scaled varved layer cake and initiate an single point failure Alsop & Marco (2011, 2013). Stratified layered sediments provide easy- slip zones along which a compressive wave spreads downslope, whereas an extensional wave propagates upslope. Extension in the upslope regime (head) is marked by normal faults and balanced by contractional folds and thrust in the lower downslope regimes (toe) Alsop & Marco (2013).

Evolution and overprinting of slumped systems can be described in different phases: intitation, translation, cessation, relaxation and compaction phases (Fig.25). Depending on extensional or contraction translation respectively cessation, four overprinting scenarios within a single event are described. (i) Whether if the head or toe is investigated (ii) or if cessation of the slump initiates at upslope or downslope regime. Alsop & Marco (2011) Structures from an individual slump horizon comprise coaxially refolded and reworked sheared folds and thrusts, both verging back up and then down the paleoslope. The reworked structures are assumed to be related to earthquake

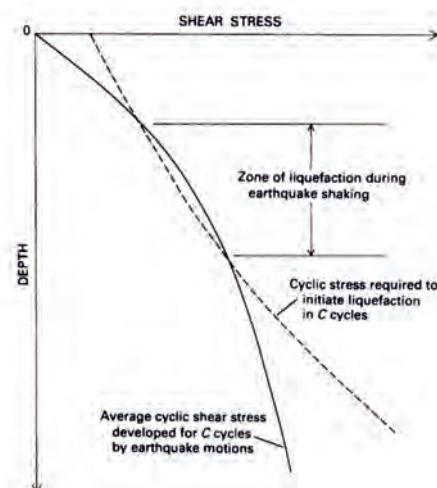


Fig. 7: Depth of liquefaction, affected by depth below surface and seismic shear stress. C, number and shaking cycles Seed, H.B., Idriss (1971).

triggered tsunami and seiche waves that flow slightly later across the main slump triggered by the same event in water depth of < 100 m, to rework the top of the entire slump. Alsop & Marco (2012b)

Slump folds bear a systematic relationship in respect to the paleoslope upon they were created. To determine paleoslopes Alsop applied frameworks developed for geometric analyses of folds and fabrics in metamorphic rocks on gravity- driven slumping structures Alsop & Marco (2013) and statistical methods Alsop & Marco (2012a). To analyze slumped folds, slumped systems are classified into coherent- (connected and orderly, bedding is intact), semi- coherent- (partially/ almost consistent, bedding becomes disturbed) and incoherent slumps (lacking in organization, bedding is disturbed), based on preserved geometries. Observed structures reflect the increasing finite state of the deformation and do not refer to the evolution of the slumped system. Within coherent systems, fold hinges and axial planes built clustered patterns. As the systems become semi- coherent and incoherent the pattern of fold hinges and axial planes become more scattered. In coherent- and semi-coherent slumps reworked patterns of Type 1, 2 and 3 refolded folds are observed. Against traditional considerations a single seismic event is capable to create refolded structures. Missing parasitic folds reflects rapid deformation and a limited viscosity contrast of the sedimentary layer-cake. As deformation intensifies within semi-coherent slumps some fold hinges rotate into the flow direction, creating sheath folds or roll down the slope and create newly classified spiral folds. Under conditions of extreme deformation semi- detached en- echelon folds develop, newly classified as X-folds. Alsop & Marco (2013)

To determine statistically the paleoslope direction five different methods were applied and more than 350 folds were documented:

- Mean axis method (MAM): gives relationship of slump folds and paleoslope
- Mean axial plane strike method (MAPS): determines the transport direction
- Mean axial-planar method (MAD): utilizes trend of fold hinges together with angle of dip of axial fold plane to determine paleoslope
- Separation arc method (SAM): based on highly variable hinge orientations of folds about the paleoslope direction
- Axial-planar intersection method (AIM): utilizes statistical orientation of fold axial planes to determine trend and direction of flow

The authors recognized with these techniques large-scale radial slump system directed to the depocenter of the Dead Sea. Investigations support flow perturbation models, where transport-normal fold hinges are generated by layer- parallel shear (LPS). Alsop & Marco (2012a)

To observe traces of earthquakes in sediments, finely laminated varve like deposits are regarded as most suitable (Becker *et al.*, 2006). Varved sediments define a stratigraphic template and allow relative age dating. Each varve is therefore considered as annual laminae and used to date the period of sedimentation and the relative time in between the single seismic events (Rodríguez-Pascua, 1996). If a vertical cross section of clastic sediments are furthermore eroded by a brook the perfect environment is maintained to study soft-sediment deformation. Sedimentary archives are for that reason an important access to determine the reoccurrence of paleoearthquake activity. Another reported spot where those conditions are fulfilled and similar structures within a cave can be found is in the Sous-les-Sangles Vaace in the southern Jura Mountains (Lignier & M.Desmet, 2002).

If during seismogenic triggering the fine laminated varved sediments are kept under highly water saturated conditions, they are favorable to undergo liquefaction (Fig. 9). Liquefaction is understood to be a process where saturated sediments temporarily lose strength due to earthquake ground shaking resulting in instabilities. (Tuttle, 2001) Fluidization and liquefaction are attributed to pore pressure changes caused by fluid escape and hydrodynamic instabilities within the sediments.

The deformed strata most likely develop at the water-sediment interface (Marco *et al.*, 1996). With increasing depth the higher static vertical effective stress (total overburden pressure minus pore-water pressure) and the resistance of the sediment to shear increases and makes liquefaction more unlikely (Obermeier, 1996).

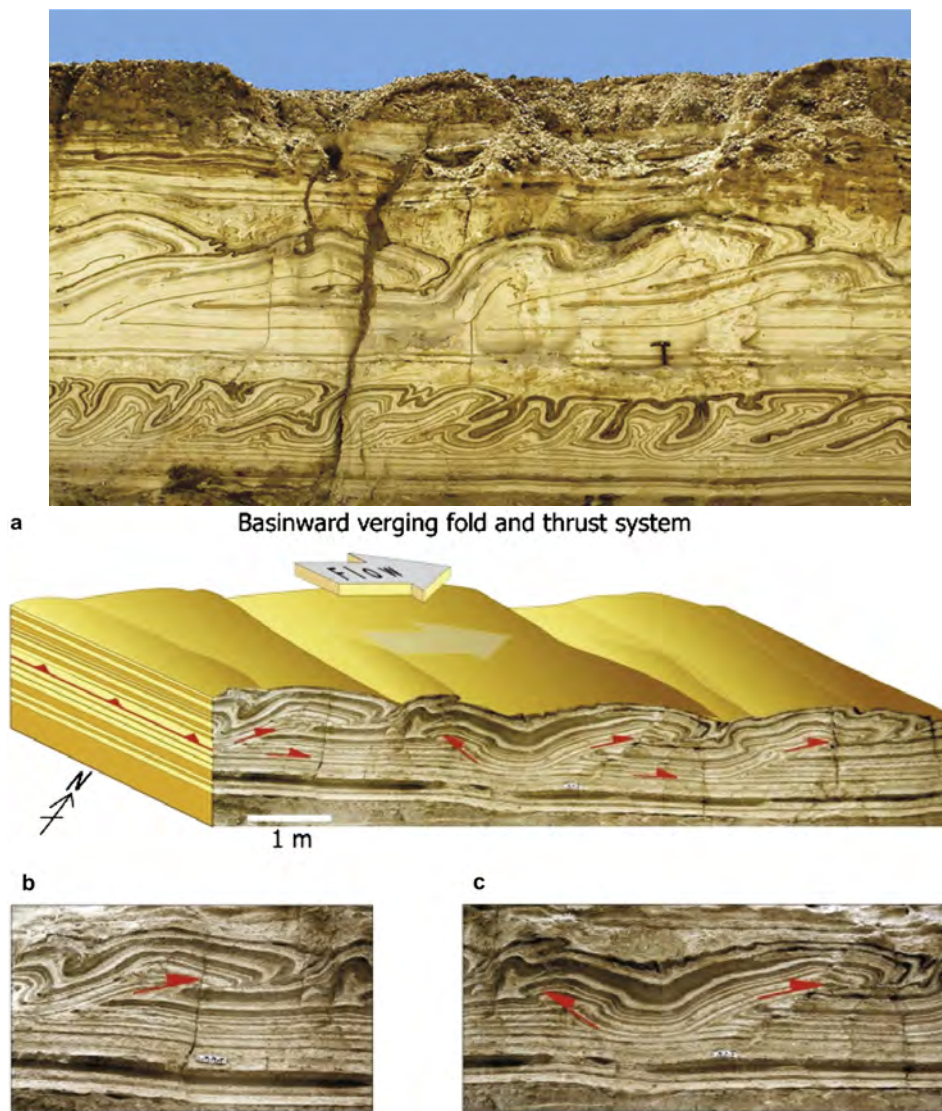


Fig. 8: Geometric analogies from the Dead Sea Basin Alsop & Marco (2011)

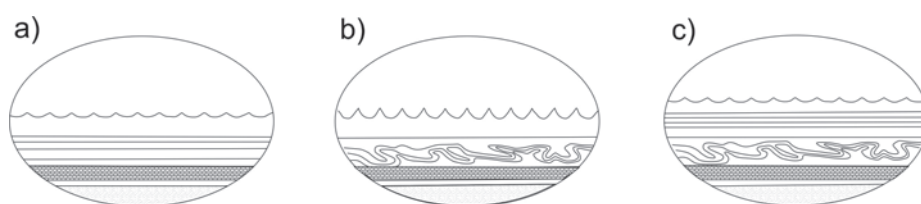


Fig. 9: (a) fine-grained varved deposition. (b) seismic triggered soft-sediment deformation caused by liquefaction in the uppermost highly water saturated layers (c) continuous sedimentation after Becker *et al.* (2006).

METHODOLOGY

4.1 OUTCROP ANALYSIS

Detailed field analyses of unconsolidated sediments have been made in the Hirlatz Cave from the 27.05. to 28.05.2013. The crew consisted of Bernhard Grasemann (supervisor), Lukas Plan (supervisor), Martina Lan Salomon (master student), Harald Bauer, Katharina Böhm and Thomas Exner.

The field trip started from the Simony-monument in the Echerntal. Right above the Echerntal the cave entrance is situated at an elevation of 870 m ASL in the north face of the Hirlatz. The outcrop wall can be found 2.8 km SE from the cave entrance. The way to the study site in the Lehmklamm starts at the Zubringer, which connects the entrance with Alter Teil. And continued via Östl. Blocktunnel, Riesenklamm, Sandtunnel, Aufsteigender Tunnel to the August Hödl-Halle to the Lehmgleitscher into the Schwarze Halle and Bohnerzhalle. Shortly before Sandtunnel the lowest point on the way to the outcrop with 846 m can be found. Into NW- direction towards Trichtergang and S-Gang a biwak was arranged in the Brückenhalle. The Brückenhalle is with an elevation of 1027 m the highest point on the way to Lehmklamm.

Via Lehmtunnel the way leads from the Brückenhalle to the outcrop wall in the Lehmklamm. There clastic deposits, which have been cut by a brook can be found. The outcrop analysis were done by detailed observations as well as measurements of structures. Furthermore 11 unoriented samples were taken from different layers for sedimentological lab analysis, source-rock determination and for micro-structural investigations.

4.2 X-RAY DIFFRACTION (XRD)

Bulk rock and clay mineral analyses were carried out with XRD on dry and powdered samples. The samples were dried at 60 °C overnight. For the bulk mineralogy samples HI 2 to HI 4 and HI 6 to HI 9 were first ground by hand with an agate mortar and pestle, until a homogeneous powder was obtained. The processed samples were then placed in a sample holder and analysed.

To separate the clay fraction for XRD analysis organic matter was removed. Samples HI 7 to HI 9 were mixed with an dilution of hydrogen peroxide H_2O_2 and H_2O ; in a ratio 1:1. The reaction took place for 21 days. For further disaggregation the samples were treated for 5 minutes in a ultrasonic bath. Afterwards Na-tripolyphosphate was added to the suspension to avoid agglomerates. They could cause convection and disturb the sedimentation.

For collection the clay size fraction ($< 2 \mu\text{m}$), samples were filled into an Atterberg cylinder and sedimented for 24 h and 33 min at a temperature of 20 °C, with a drop height of 30 cm. Stokes' law is describing the time a particle with an distinct diameter and density needs to sink down in an liquid with defined density. This principle is used in the Atterberg apparatus, which consists of a glass cylinder (Fig. 10). Sample HI 7 caused some problems, because the clay particles flocculated. Some more Na-tripolyphosphate was added and the sedimentation in the Atterberg cylinder was repeated under the same conditions.

After the $< 2 \mu\text{m}$ fraction was extracted, the samples were dried for 24 hours at 60°C. The samples for the clay mineral analysis were also homogenised in an agate mortar. 50 mg of each sample were saturated with either potassium chloride (K) or magnesium chloride (Mg) and permanently shaken for 24 hours.



Fig. 10: Atterberg cylinder.

To remove the salts, samples were twice centrifuged twice. The first time for 5 min and 1500 rotations per minute (RPM) and the second time washed with distilled water and centrifuged for 10 minutes at 4000 RPM.

The K- and Mg saturated samples were sedimented on glass slides (8 mg/1 ml) and air dried at the air over night. The K saturated samples were afterwards treated with ethylenglycerol the Mg saturated samples with glycerol. Additionally, the K-saturated samples were heated up to 550 °C. Reason for the treatments is to identify expandable clay minerals.

The X-ray diffraction analyses were carried out with a PANanalytical PW3040/60 X'Pert PRO diffractometer using copper K α radiation at 40 kV and 40 mA. All specimens were run at a 2θ -angle ranging from 2 ° to 70 °(40 °) with a step size of 0.0167 and a scanning speed of 5 seconds per step. For the interpretation the PANanalytical X'Pert High score plus software was used.

Principle of X-ray diffraction is the Bragg's Law $n\lambda = 2d\sin\theta$, describing the relationship between the wavelength of the X-ray beam at a certain angle of incidence (θ) and the lattice spacing within the crystal. X-rays are generated in a cathode ray tube, filtered to produce a monochromatic beam and concentrated on the sample. The incident X-rays interfere with the crystals and produce a constructive inference pattern if the Bragg's law is fulfilled. The diffraction pattern provides a characteristic fingerprint of the different minerals, and allows to identify them.

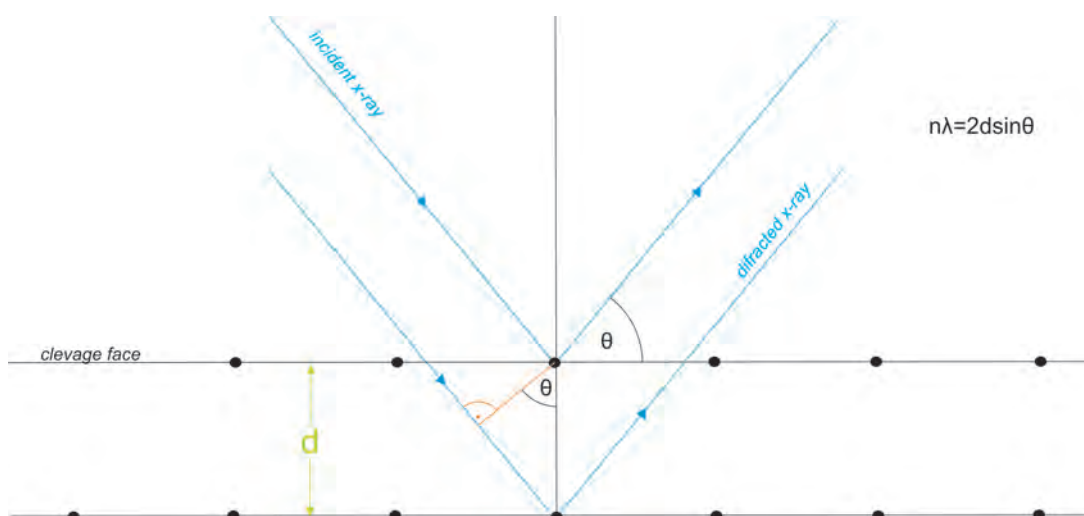


Fig. 11: Bragg's law; λ ...wavelength; d ...lattice plane distance; θ ...incidence angle; n ...integer.

4.3 HEAVY MINERAL ANALYSIS

Heavy mineral analysis were implemented to get an idea about the source rock and the source area where it derives from. It is most often the accessory minerals that help to determine the sediment's provenance. Therefore the coarse grained samples HI 2, HI 3 and HI 4 were investigated.

First of all the samples were decarbonized with diluted acetic acid and sieved, the fraction from 0.063-0.4 mm is used for further analysis. Afterwards the sieve fraction was dried at 60 °C. In the next step the heavy minerals were separated with the heavy liquid 1,1,2,2,- tetrabromethane (C₂H₂Br₄), which has a density of 2.94 kg/dm³ at 20 °C. The separation with tetrabromethane is based on the specific gravities of different minerals. The heavier minerals will sink because of their higher specific gravity (> 2.9 kg/dm³) and the lighter more common minerals like quartz, feldspar and calcite (~ 2.9) will float. Afterward the separated heavy minerals were imbedded in Canada balsam and analyzed under the optical microscope. For classification around 100 minerals and another 30 grains were counted for the backup in each section.

4.4 STRUCTURAL ANALYSIS

Photos from the field were used with the assistance of CorelDraw X5 to quantify the different deforming structures. Thinsections were prepared from samples taken in the field and analyzed down to microscopic details under an optical microscope. Aim of those observation are there appearance and to understand how the structures were formed. Most observed features range in the dimension of millimeters to a few centimeters. Therefore shortening (s) of folds was calculated with following formula

$$s [\%] = \frac{l_0 - l}{l_0} * 100$$

The simplest form to make this calculations to reconstruct the length before deformation (l_0) and measure the actual length (l) of the linear structure.

To quantify extensional features a similar formula was applied $e [\%] = \frac{l - l_0}{l_0} * 100$. Once more l_0 and the actual length l was measured.

For quantifying boudins it is not enough to only measure the length (L) and calculate the extensional component. So far even for the simplest system of symmetric boudins no consistent nomenclature has been adopted in the literature (Goscombe *et al.*, 2004). It is also of importance to measure the width (W), the offset (D), the aperture angle (α) and the rotational angle (Θ). With those parameters the aspect ratio (L_R) can be calculated. During boudinage a competent layer is broken up into more and more small separated sections until a characteristic width to length ratio, expressed by the aspect ratio. Which should give us an idea of the shape of the boudins and reflects the competence and viscosity contrast during deformation (Fig. 14). Aspect ratio/Shape factor can be defined as $L_R = \frac{L}{W}$ (Passchier & Druguet, 2002). Standard values for the aspect ratios ranging between 2 and 4. Hans Ramberg found that the competent layers form the most rectangular boudins, whereas more incompetent layers are most likely to form pinch and swell structures. (Fossen, 2012)

Furthermore the fault system polarity (P) is considered. The Displacement vector (D) consists out of two different components, the heve (H) and the throw (T). P shows values from -1 to 1 The fault system polarity should give an idea, whether the faults separating the boudins are dipping into a specific direction or if their dip direction is distributed symmetrical. (Fig. 13 and Fig. 15) The polarity is calculated by dividing the sum of throws by the absolute sum of the throw

$$P = \frac{\sum T}{\sum |T|} \quad (\text{after Ishikawa \& Otsuki (1995); Moriya et al. (2005)})$$

With the measured parameters determination of the coefficient of variation is possible. The coefficient of variation is calculated to understand if the faults separating the boudins do cluster or not, by calculating the standard deviation of the length $\sigma(L)$ of the boudins and the mean of the lengths $\mu(L)$ and dividing those two amounts. $CV = \frac{\sigma(L)}{\mu(L)}$ Values for the coefficient (CV) can be bigger or smaller than 1. Meaning that values for the CV bigger than one do cluster, whereas values smaller than one do not cluster. (Fig. 16)

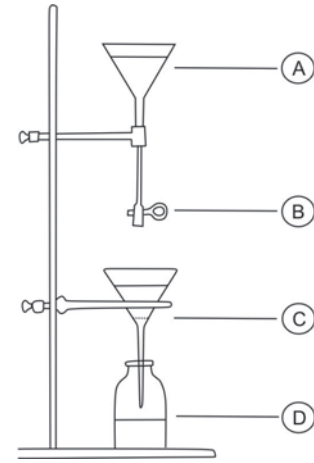


Fig. 12: Apparatus for heavy mineral separation A. funnel with heavy liquid tetrabromethane B. rubber sleeve and pinch cock C. funnel and filter paper D. collecting tray.

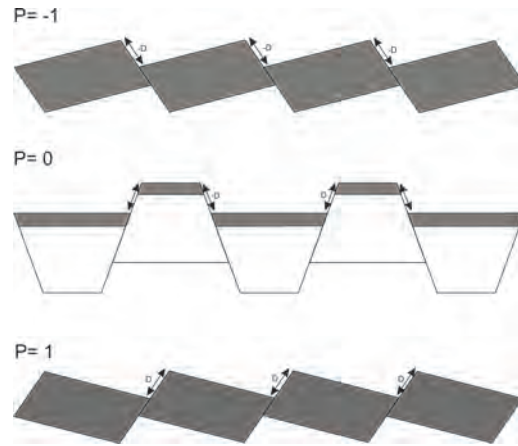


Fig. 13: Fault system polarity shows values from -1 to 1, P=-1 all faults dipping to the right P=0 amount of left and right dipping faults equal distributed P=1 faults dipping to the left.

Undeformed fluvio-lacustrine varve-like strata between the deformed ones were first determined as annual structures and counted. With this method we hope to estimate the time between the single seismic events. Therefore layers were counted macroscopically and in the thinsections and then divided by two. The reason for dividing the amount of layers by two is that an internal seasonal layering is expected. The varve counts were replicated and measured on 5 different spots in the outcrop wall projected and extended to estimate the sedimentation duration and the time between the earthquakes.

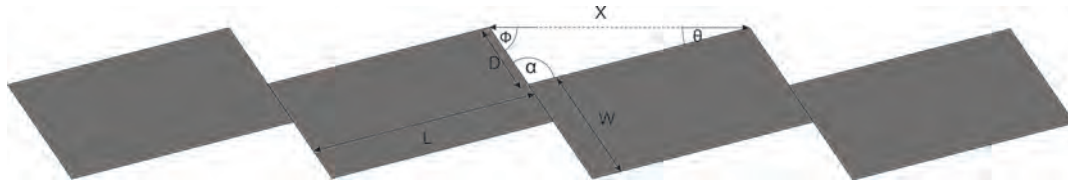


Fig. 14: Parameter to quantify Domino-boudins: L...length W...width D...offset α ... aperture angle Θ ...rotational angle.

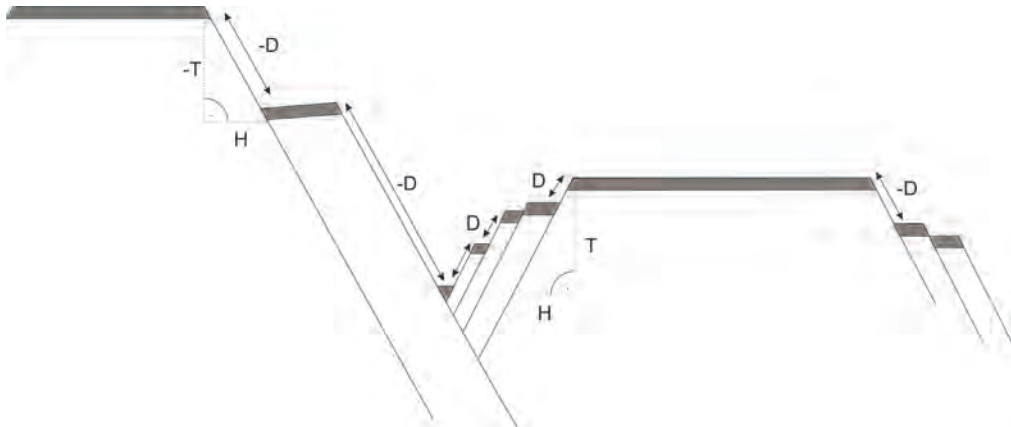


Fig. 15: Fault system polarity: D...displacement fault dipping towards the right -D...displacement fault dipping towards the left T...throw H...heave.

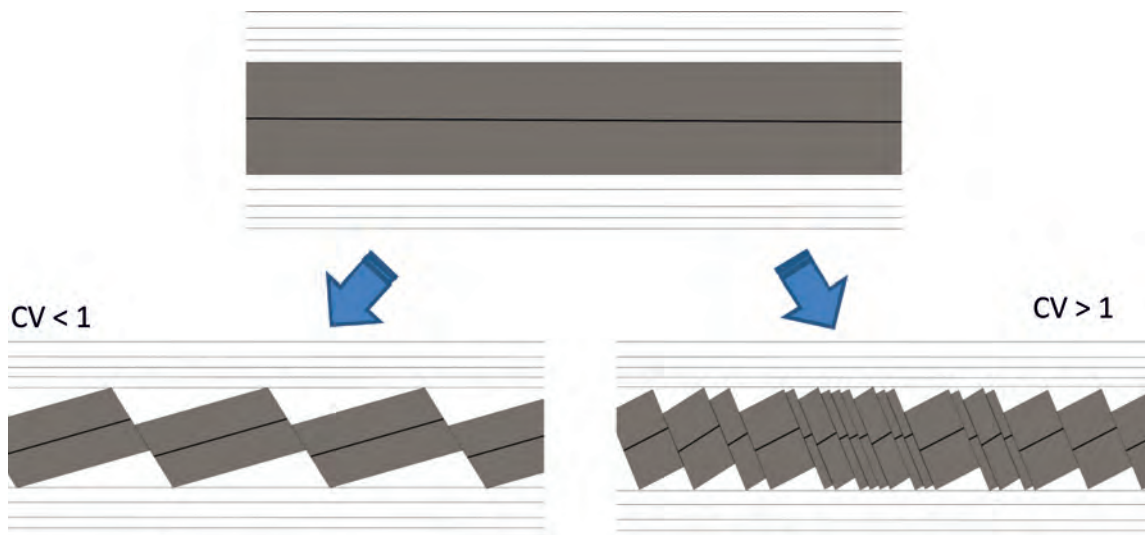


Fig. 16: Coefficient of variation, where $CV < 1$ do not cluster and $CV > 1$ do cluster.

RESULTS

5.1 SEDIMENTOLOGICAL OBSERVATIONS

Sedimentological investigations were undertaken and of interest to estimate (i) first of all the mineralogical composition of the sediments, (ii) to see if there is an significant difference in between the darker and brighter deposits and of course to (iii) estimate a potential source area of the sediments.

5.1.1 Bulk composition under the XRD

The mineralogical composition of 7 different bulk samples was examined with XRD and are shown in Fig. 17. Sample HI 2 is taken from the sandy detachment zone of an listric fault. HI 3 was sampled from a sandy current ripple from the very top of the outcrop wall. Probe HI 4 is taken from the very top of the outcrop wall, this sample is coarser grained than HI 3. HI 6 is a calcareous cover from the top of the outcrop. Samples HI 7, HI 8 and HI 9, were each taken from a bright, a dark and a lightly brown layer. HI 7 originates from an light layer, HI 8 represents a dark layer and sample HI 9 is neither very dark nor bright, it can be described as light brown.

In general, the composition of the single layers is pretty similar. The brighter and darker layers consist mainly of calcite, quartz, dolomite, ankerite, muscovite, chlorite and biotite and minor amounts of K-feldspar. In the darker layers, the amount of carbonate is reduced and K-feldspar is missing. Darker layer contain more mica and brighter layers are quartz and carbonate enriched.

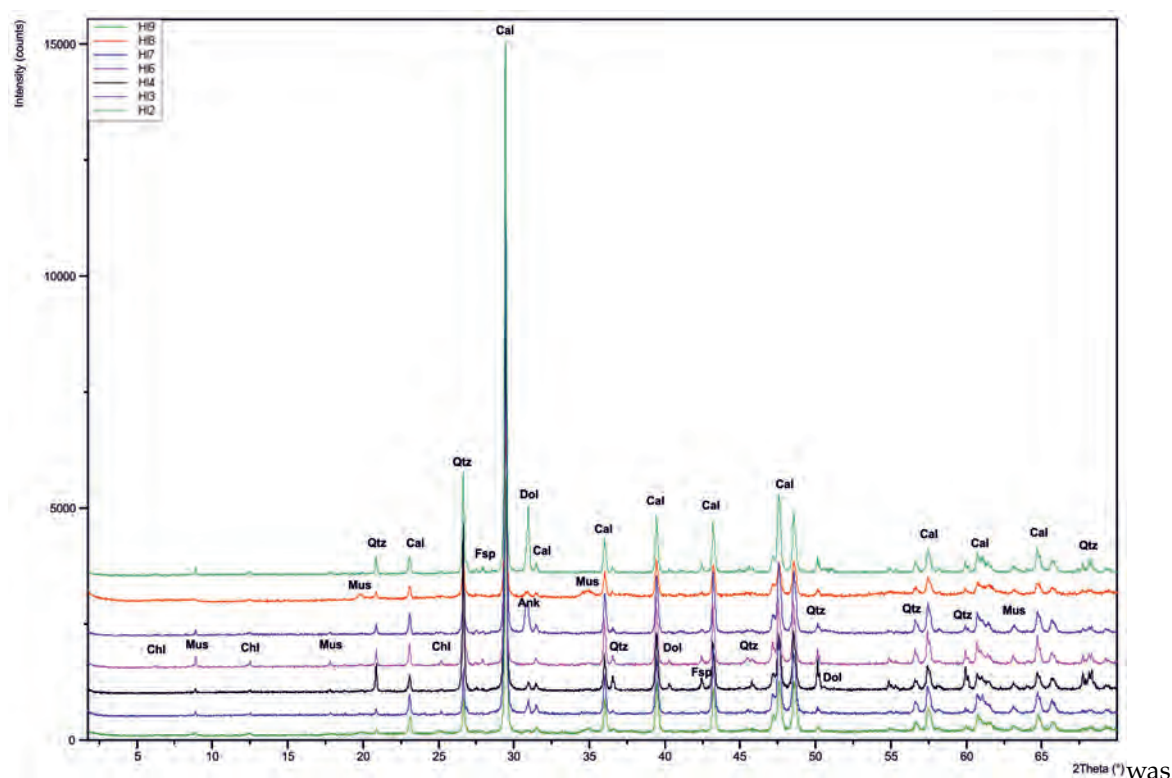


Fig. 17: Bulk mineralogy; X-ray diffraction patterns: HI 9...middle brown clay-sized layer, HI 8...dark clay-sized layer, HI 7...bright clay-sized layer, HI 6...calcareous cover, HI 4...coarser grained (maybe Augenstein) from top, HI 3... fine grained sandy sample from current ripple, HI 2... fine grained sand detachment zone.

5.1.2 Clay mineral analysis (<2 μm fraction)

2 μm fraction of samples HI 7, HI 8 and HI 9 was investigated with XRD to obtain more information about the mineralogical composition of the varvelike deposits. Once more we find a pretty similar composition within the different layers consisting of the clay minerals illite, smectite, chlorite and kaolinite. Differences are like in the bulk composition analysis just found in the quantity of the minerals. In Fig. 18a,b, and c, x-ray patterns of samples HI 7, HI 8 and HI 9 are shown. Saturation with magnesium and glycerin, shows that the peak of vermiculite d (001) remains at its position of 14,5 Å and that smectite expands from 14,5 Å to 17,5 Å. To be sure that no vermiculite can be found in the samples, treatment with kalium and ethylenglycol were operated, vermiculite remains with its position at 10 Å and smectite expands again to 17 Å. To distinguish vermiculite from chlorite samples were also treated with potassium and were tempered. Vermiculite would collapse to 10 Å, whereas chlorite stays at 14 Å.

Fig 18c, represents the magnesium saturated patterns to compare the samples with each other. HI 7 (blue line) originates from an light layer, HI 8 represents a dark layer and sample HI 9 is neither very dark nor bright, as in the bulk composition.

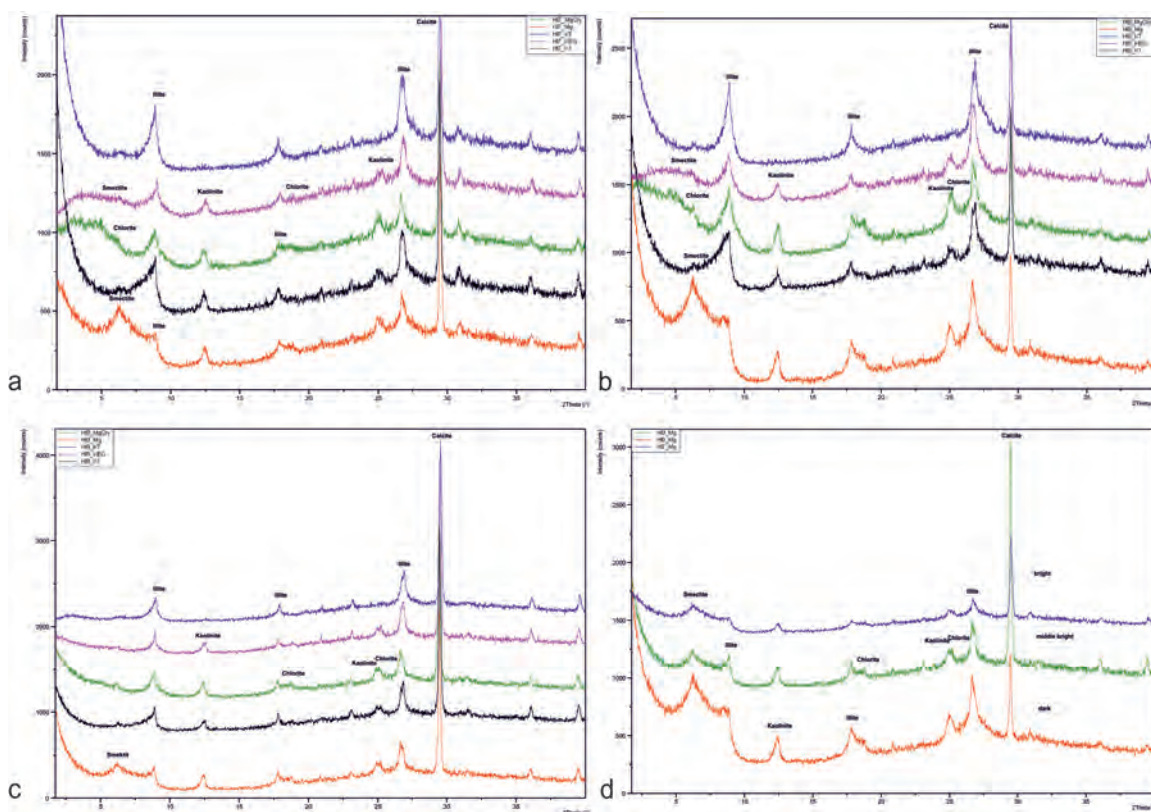


Fig. 18: Clay mineral analysis: Samples were treated in 5 different ways to distinguish different clay minerals. **blue** graph with MgGly...Magnesium Glycerin, **purple** saturated with Mg...Magnesium, **green** with KT...Kalium and tempered at 550 °C, **black** with KEG...Kalium Ethylenglycol, **red** with K1...simply saturated with Kalium. a) shows sample HI 7. b) graphs of sample HI 8. c) X-ray diagram of sample HI 9. d) comparison of samples HI 9, HI 8 and HI 7.

5.1.3 Heavy Mineral analysis

Heavy minerals found in the interbedded fine grained sandy layers consist of major amounts of epidote (~ 40 %), zoesite (~ 20 %), zircon (~10 %) and minor amounts of garnet (~ 7 %), chloritoid (~5 %), rutile (~4 %), tourmaline (~4 %), kyanite (~4 %), apatite (~3 %), hornblende (~2 %) and staurolite (~ 1/4 %). HI 3 is a sandy sample from current ripple at the very top of the outcrop wall. Here apatite is completely missing (Fig. 19a). In Fig. 19b, sample HI 2 is shown, it originates from a finely grained sandy detachment zone. HI 4 was also sampled from a small depression at the top of the outcrop wall. In HI 4 (1) no apatite was found but it shows the existence of staurolite. In general we can say, that in HI 4 much more garnet was counted, than in the finer grained sandy layers from the top of the outcrop and from the detachment zones.

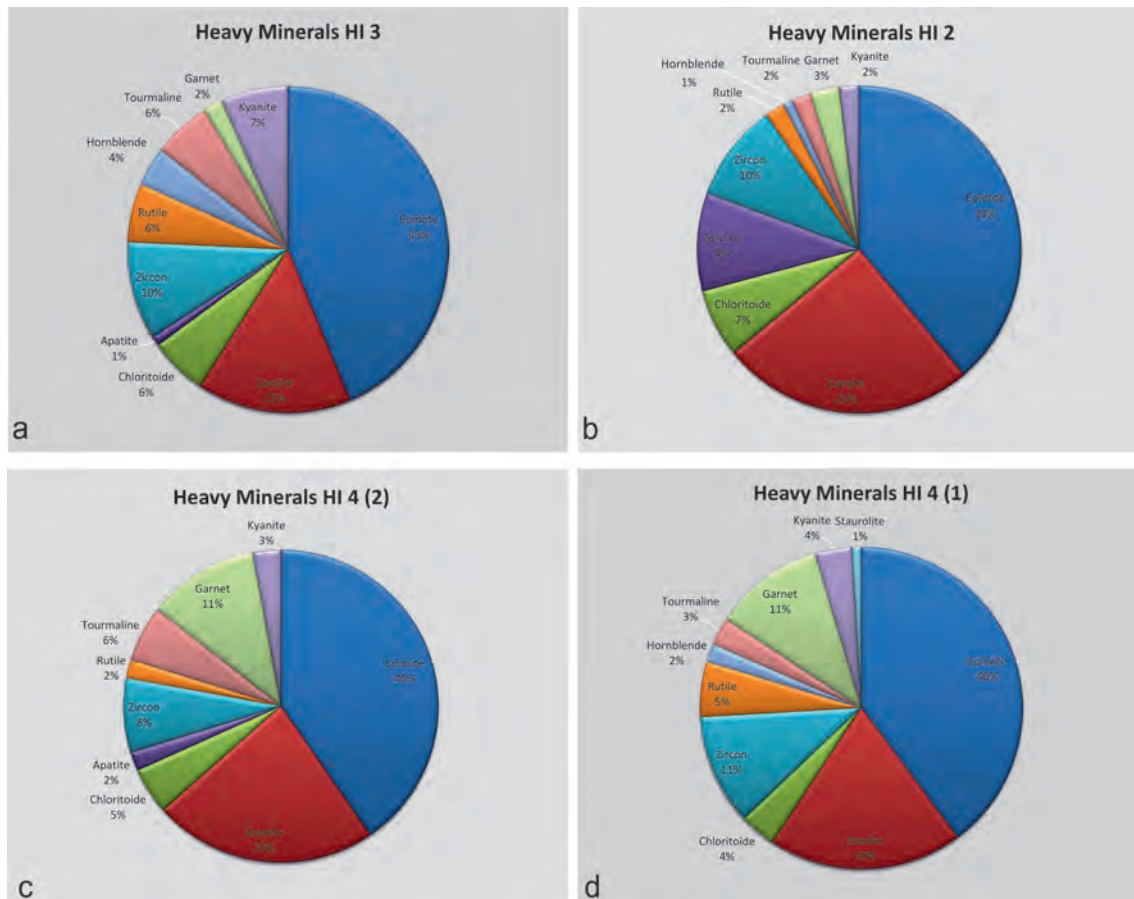


Fig. 19: Heavy mineral analysis: a) HI 3... fine grained sandy sample from current ripple. b) HI 2... fine grained sand detachment zone c and d) HI 4...coarser grained (maybe Augenstein) from a depression at the top of the outcrop wall.

5.2 STRUCTURAL ANALYSIS

Soft sediment deformation structures have been observed horizontally in the cave sediments between undeformed strata. Millimeter to centimeter sized seismogenic induced flamwase and fishtail like structures, domino-boudins and syn-slumping structures such as folds and faults have been found in different stratigraphic horizons. Stratigraphy is provided by a fine laminated layer-cake, which are extremely effective to record effects of deformation. Structures are underlain and overlain by horizontally laminated undeformed layers. The cave preserved exceptional sedimentary features from erosion and bioturbation in the approximately 6.8 m times 3 m big NE-SW striking outcrop wall. In the next sections the different structural features are gonna be described.

5.2.1 Current ripples

Observation of coarsening upward into sandy layers on top of the outcrop wall has been made. In the sandy parts current ripples indicate a north-directed paleo flow under phreatic conditions (Fig. 20a,c). At the luv side much more darker and heavy minerals are deposited than on the lee side. This indicator helps us to interpret the pale-flow direction. The paleo-conditions are different to the current flow direction in the Lehmklamm. Nowadays the flow of the vadose water in the cave is south directed. A few centimeter underneath the top of the outcrop wall we observed a fault-bend fold, which has been deformed into an antiformal stack. . Axial plane of the fault-bend fold is steeply dipping towards the SW (300/85) with an gently NE dipping fold axes (023/05). Single layers within the duplex showing shortening ranging between 5.1 % and 7.2 %.

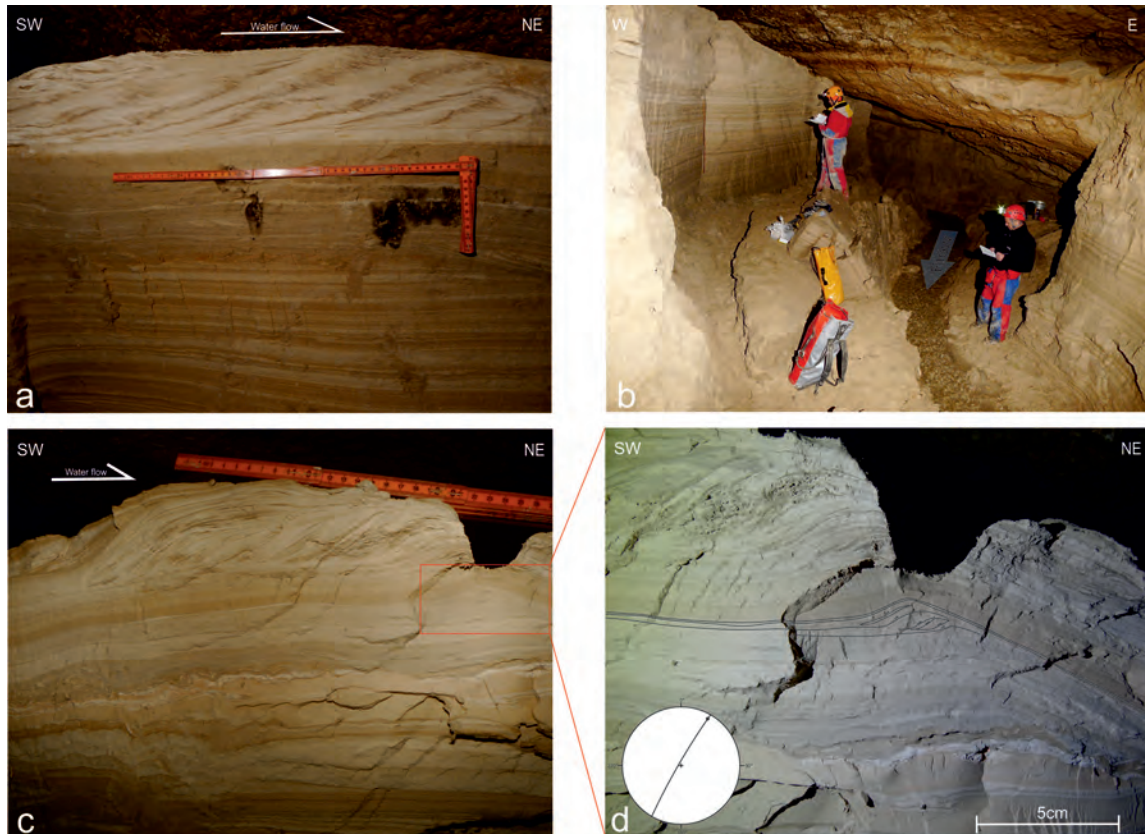


Fig. 20: a) current ripple indicating north directed paleo flow; Photo by L. Plan b) actual current with south directed flow; Photo by Lukas Plan c) current ripple: north-wards flow; Photo by L. Plan d) duplex with steep SW dipping axial plane (300/85) and gently NE dipping fold axes (023/05); Photo by B. Grasemann.

5.2.2 Water escape structures

Billow- like folds with flame-like, wavy or fishtail-like symmetry have been examined. Heifetz et al. (Heifetz *et al.*, 2005) described similar structures at the Dead Sea. He found conspicuous analogies to Kelvin-Helmholtz Instabilities, which are well known from e.g clouds (Fig. 21) and has convincingly tied them to earthquakes. Lighter carbonate (calcite: $\rho=2.71$ g/cm³; dolomite: $\rho=2.84$ g/cm³; ankerite: 3.05 g/cm³) and quartz ($\rho=2.62$ g/cm³) enriched layers overlies the heavier clay detritus enriched layers (muscovite: 2.82 biotite 3.09 chlorite 2.6 - 3.3 g/cm³). The darker heavier layers intrude in the brighter and lighter ones. Within the dark intrusion



Fig. 21: Kelvin-Helmholtz Instabilities in clouds, conspicuous analogies to sedimentary flame structures Kaushik (2013).

turbulence and a mix of brighter and darker deposits can be observed. Such folds occur due to layer-parallel displacement, where the lighter layer overlies the heavier one. Layers are moving horizontally into the same direction with different velocities creating shear in between them. Shear in turn causes instabilities and gives rise to the gravitational heavier layer, the denser layer tends to intrude into the lighter one and mix with it. (Heifetz *et al.*, 2005)

The amplitude of the wavy structures ranges between 8.2 mm and 20.9 mm with an wavelength about 16.3 mm. Structures display shortening of 46.8 % at Fig. 22d, 54.5 % at Fig. 22c, and 22.2 % at Fig. 22a.

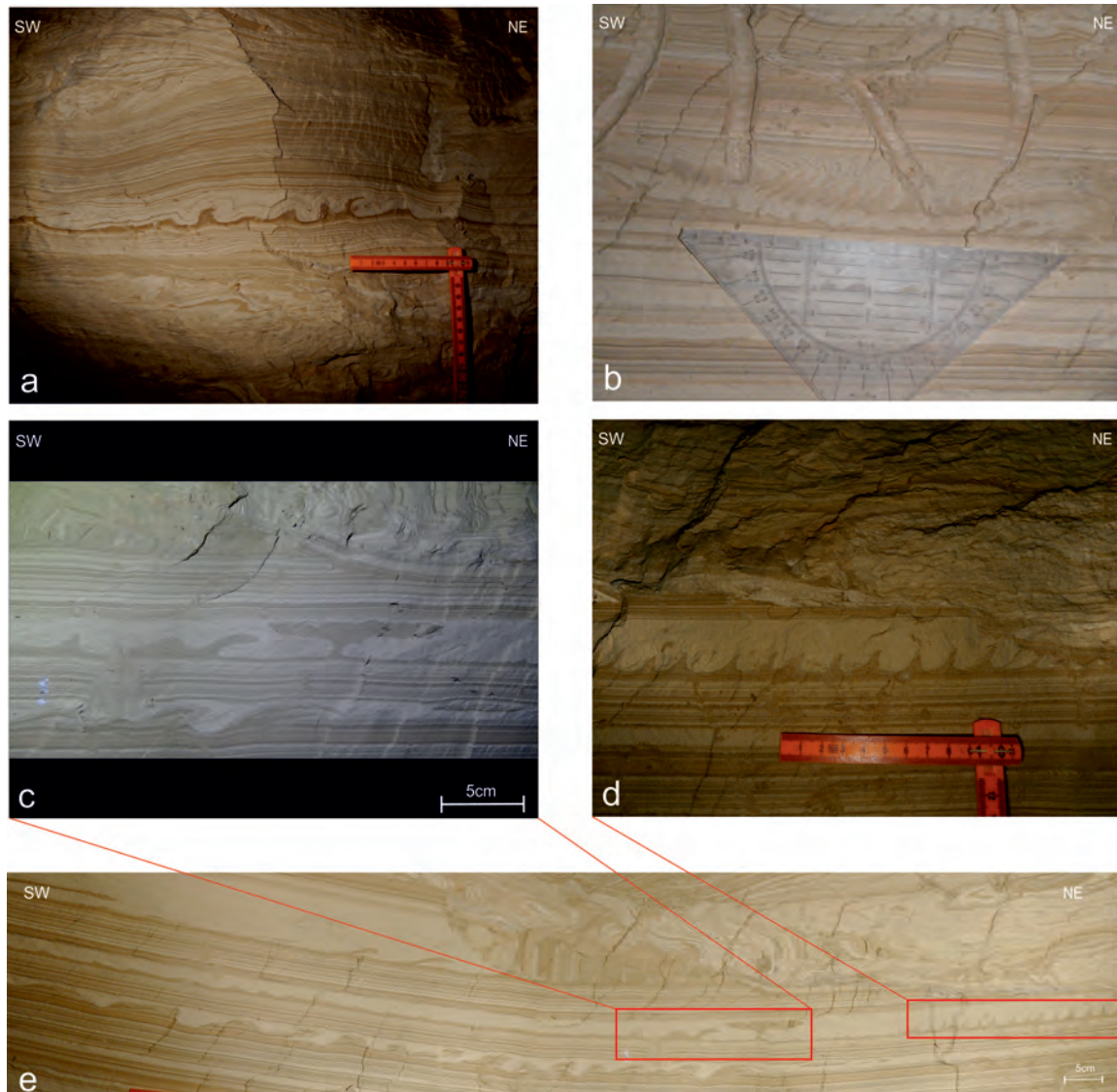


Fig. 22: a) intruded cusps representing 22.2 % shortening, Photo by L. Plan b) flame structures c) fishtail and flame structures with cusps and turbulent structures accomadating 54.5 % shortening, Photo by B. Grasemann d) intruded flames 46.8 % shortening, Photo by L. Plan e) structures c, and d, occuring in one stratigraphic level, Photo by L. Plan.

5.2.3 Syn-slumping faults and folds

Various numbers of mechanism lead to formation of fold and faults: seismicity, an increase in pore fluid pressure and gravity driven slumping. An increase in pore fluid pressure, reduces the shear strength of sediments dramatically (see 3. Speleoseismology). Hence gravity driven slumping and soft sediment deformation may be triggered.

Slumping is considered to initiate at a single point generating a compressive wave. The wave starts to propagate down- and upslope marked by extension in the upslope regime and by contraction at the toe of the slump. (Farrell, 1984)

The geometries of the deformation structures reflects the paleoslope upon which soft sediment deformation was created. Conspicuous analogies to the below described structures can be found in the Late Pleistocene Lisian Formation in the Dead Sea Basin (cf. (Alsop & Marco, 2011, 2012a,b, 2013)). At the topmost part of the outcrop wall two generations of extensional features developed with a listric geometry above an erosive base (Fig. 24, grey). Fault planes are shallow to moderately dipping (15° - 35°) towards the N and NE, respectively. Dip of the faults decreases downwards, till they flatten into underlying detachments. Geometrical the curved faults can be described with their concave side upward and downwards flattening, the shape might remind of a shovel. Intersection and offset of the faults let us assume their relative relationship. The older listric fault (Fig. 24, green) is cut by a younger extensional fault with listric geometry (Fig. 24, red), which offsets the older feature by 22 cm.



Fig. 23: Conspicuous analogies in mm-scale to observation in 24, unoriented sample.

Coupled with this listric fault a fold generated during active slumping, at the right most part of the fault (24). Axial plane of the syn-slumping fold is moderately dipping towards the SE ($161/19$) with a shallow inclined fold axes towards the SW ($210/10$).

Classical the dip direction of the axial plane is considered to indicate the upslope direction of the paleoslope. Thus the fold hinges form parallel to the strike of the slope. (Woodcock, 1979) The described pattern are only generated during strike-slip movement dominated by layer-parallel shear (velocity gradient along the flow direction), such that displacement is relatively equal along an underlying detachment Alsop & Marco (2011). If subsequent rotation or displacement like in this special case takes place, this simple pattern will get more complicated.

Due to rapid flow above the erosive base and detachments zones of the listric faults the single strata seems to be chaotic and makes it hard to recon the correlation between them.

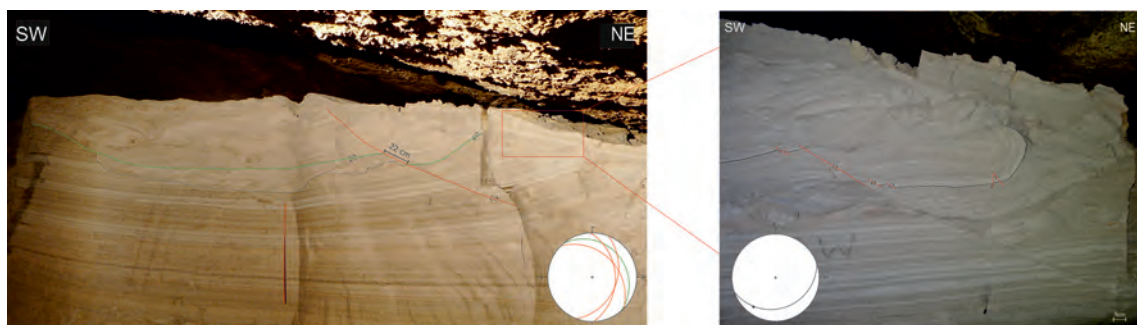


Fig. 24: Erosive base (Grey) and two generations of listric faults, younger fault (red) cuts through the older fault (green) moderately dipping towards the N and NE, respectively; slumping fold generated during activation of green listric fault, fold plane dipping moderately towards the SE, Photo by L. Plan.

Conspicuous analogies can also be observed in thin section in mm-scale (Fig. 23). Truncation of deformed layer is observed. Due to observation of solitaire breccious clast above the erosion edge a higher flow rate is expected. Sample is unoriented, therefore no estimation about kinematics can be made.

Inbedded between undeformed horizons different folded structures appear. In Fig. 26a,b,c,d,e,f,g,h,j folds occur along a flat underlying detachment parallel to the sedimentary bedding and building

up a fold and thrust system. Slumped sub-recumbent folds are typically observed with an amplitude ranging from 14 mm to 37 mm and wavelengths between 9 mm and 52 mm. Within the folds flow perturbation can be observed. In general those contractional folds can be associated with seismogenic triggered slumping events along a gently dipping paleoslope and liquefaction.

(Farrell, 1984) suggested to characterize slump systems with an interpretation model into 3 different phases: i) initiation followed by ii) translation and a phase of iii) termination. Alsop 2011, expanded the model for the interpretation of their slumping structures in the Dead Sea (Fig. 25)

Different stages of the suggested interpretation model could have been observed in the Lehmklamm. Axial planes of sub-recumbent folds in Fig. 26a and b are dominantly oriented into an uniform direction with sub-angular fold hinges which developed during non-coaxial shearing marked by downslope verging movement in translation phase. The structures form packages less than 35 mm thick and have a wavelength from 21.5 to 48.3 mm. Structure shown in Fig. 26b accommodates 33.5 % shortening.

Further non-coaxial deformation, during the late phase of translation leads to failure of the fold limbs shown in Fig. 26c-f. Occurrence of small thrust fault displaying 3.8 % of shortening,

(Fig. 26c). Contractional faults forming an about 25 mm thick imbrication zone (Fig. 26d), which develop in response to basal fault ramping. Wavelength of faults is about 52 mm. In Fig. 26f a thrust fold with a wavelength of approximately 81 mm and an amplitude of 22 mm respectively 12 mm is shown. Within the fold syn-kinematic boudins developed.

The sub-recumbent folds, which had developed during the earlier phase of translation are refolded, creating classical refolded patterns, pictured in Fig. 26g-j. In Fig. 26g the detachment shows an obvious inclination along which slumping developed. Deformed strata containing contractional structures reminiscent of refolded folds, are truncated and overlain by undeformed horizontal beds. In Fig. 26h shortening of 62.0 % is accommodated by refolded fold type 3 structures. Axial planes of the hook folds are perpendicular to each other. Fig. 26j shows a fragmented slumping fold of refolded fold type. The structural feature is completely decoupled from its stratigraphic assemblage.

In 26j we observed another slumping fold with furcation of the axial planes, which marks development of backthrusting, displaying box folds geometries. The box fold accommodates 47.3 % shortening.

Back-thrusting may locally develop in downslope verging slumps to accommodate the local shortening. Another interpretation are progressively back-rotating and upslope verging back-folds and thrusts during piggyback thrusting. (Alsop & Marco, 2011)

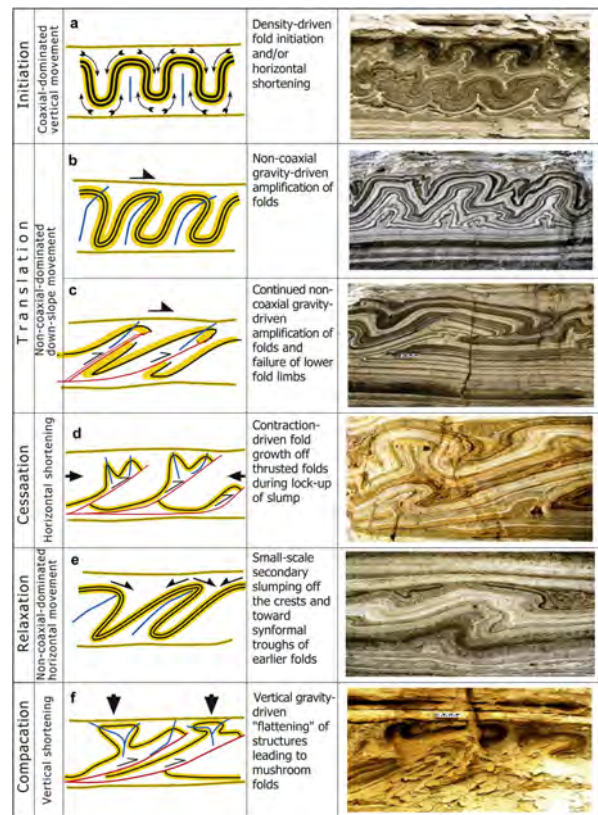


Fig. 25: Development of slump systems after Alsop & Marco (2011). Not the full range of phases are observed.

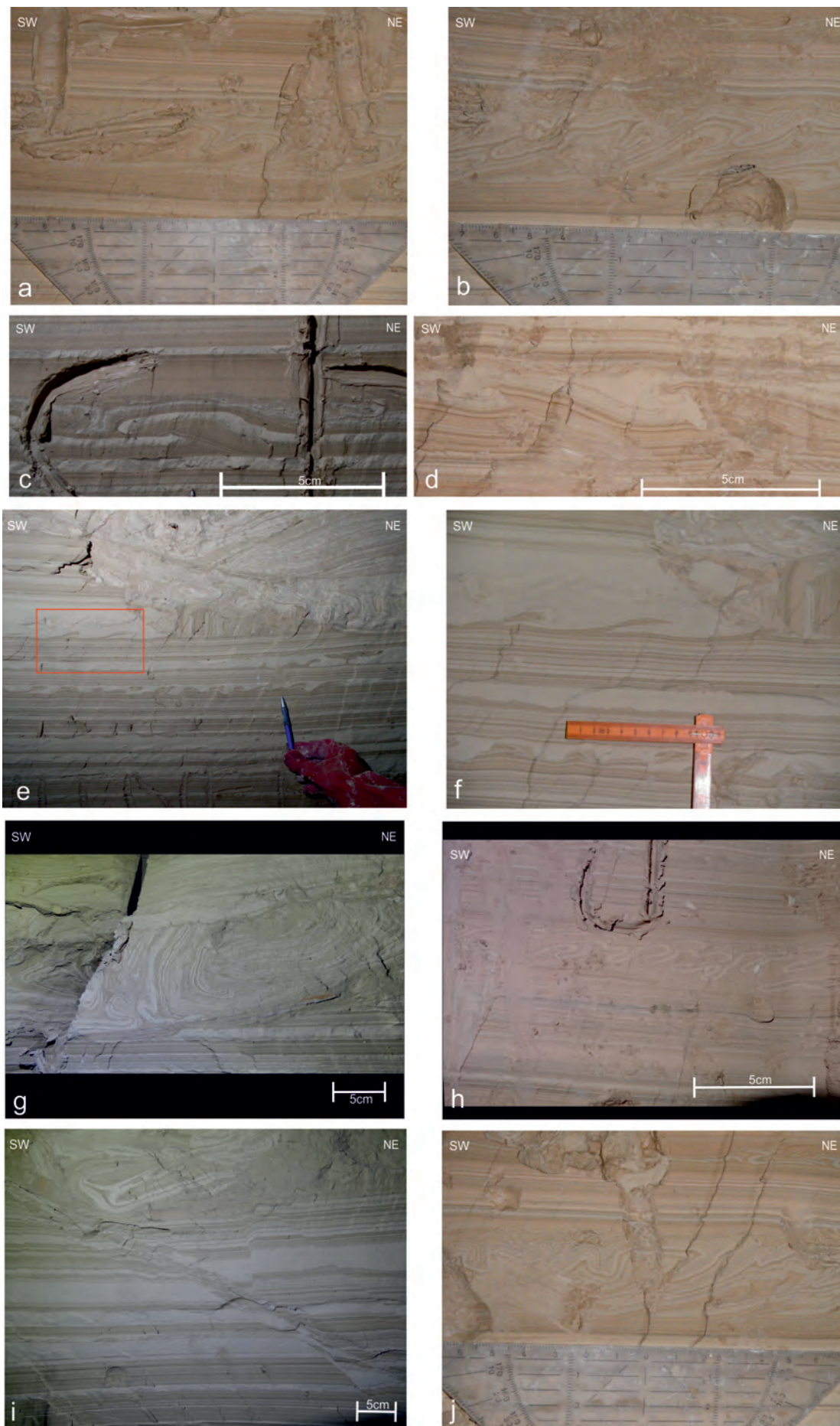


Fig. 26: Examples of slump folds. a) and b) slump fold generated during early phase of gravitational down-slope movement. c) thrust fault, 3.8 % shortening. d) imbricated thrust faults. e) & f) thrust fold with synkinematic boudins. g) SW-directed downslope slumping, with hook fold geometries. h) NE- directed downslope verging type 3 re-fold patterns. i) disassociated clast with incorporated fold. j) backthrusting detachment fold with box fold like geometry.

5.2.4 Domino-Boudins

Besides listric faults, typically for syn-slumping extension, series of simultaneously rotated normal faults can be observed. These sets of small scale extensional faults are often arranged in a line and display a symmetric domino- or bookshelf geometry. Within the footwall of individual slump systems domino boudins developed from cm- to mm- scale. Faults separating the single boudins all show a similar dip direction (SW and SSE, respectively, Fig. 29) and are assumed to have developed during cessation of slumping. As well as the faults are parallel to each other the layers within the domino boudins evolved are parallel. Offset varies marginal along the single faults and within the single deformed layers and can be assumed as constant. In Fig. 29 and different layers which are showing extension has been investigated macroscopically and microscopically, respectively in regard to the shape of the single boudins (aspect ratio), their Variation coefficient and their polarity.

Within the following 6 sampellines, representing the macroscopic measurements, 129 single boudins have been measured (Tab.1). The average length of the boudins is 9.72 mm with an spread from 1.15 mm to a maximum length of 36.73 mm. The measured thickness of the deformed layer is about 18.5 mm from 10 mm to 34 mm. (Tab.1) That leads to aspect ratios between 0.09 and 2.28 implying that the boudins are rectangular Fig. 27.

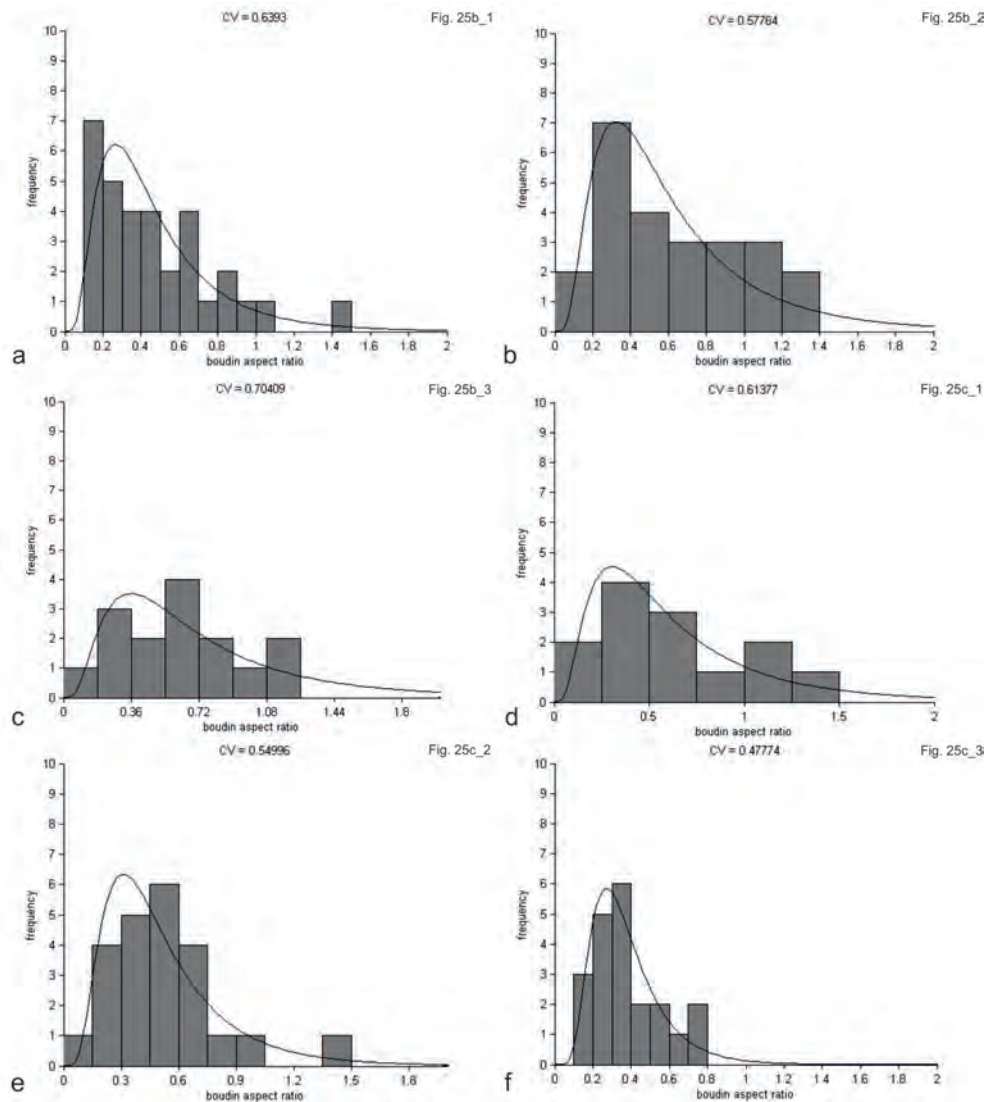
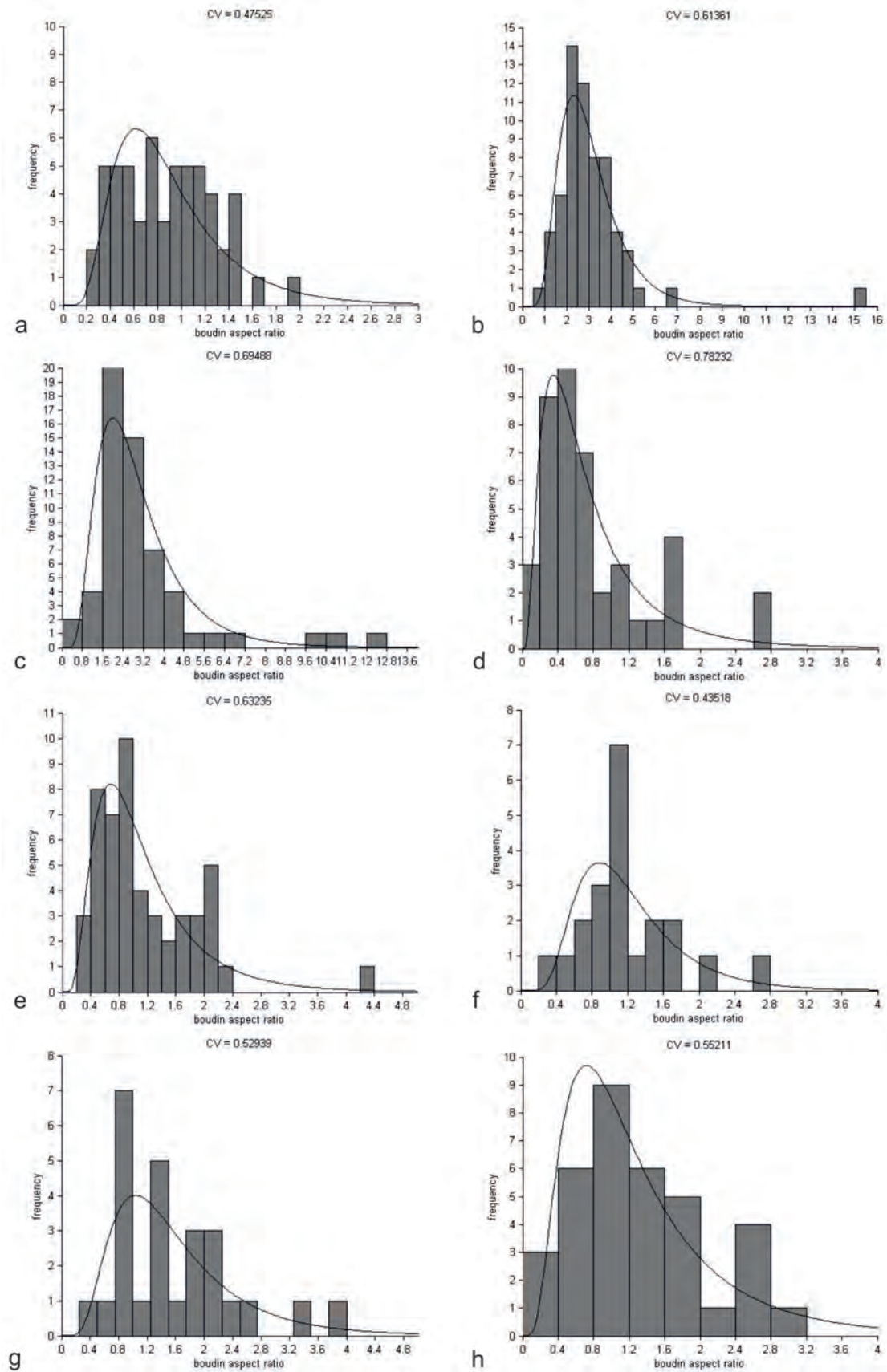


Fig. 27: Calculated aspect ratio and Coefficient of Variation: a) Layer 1 from Fig. 29e. b) Layer 2 from Fig. 29e. c) Layer 3 from Fig. 29e. d) Layer 1 from Fig. 29f. e) Layer 2 from Fig. 29f. f) Layer 3 from Fig. 29f.



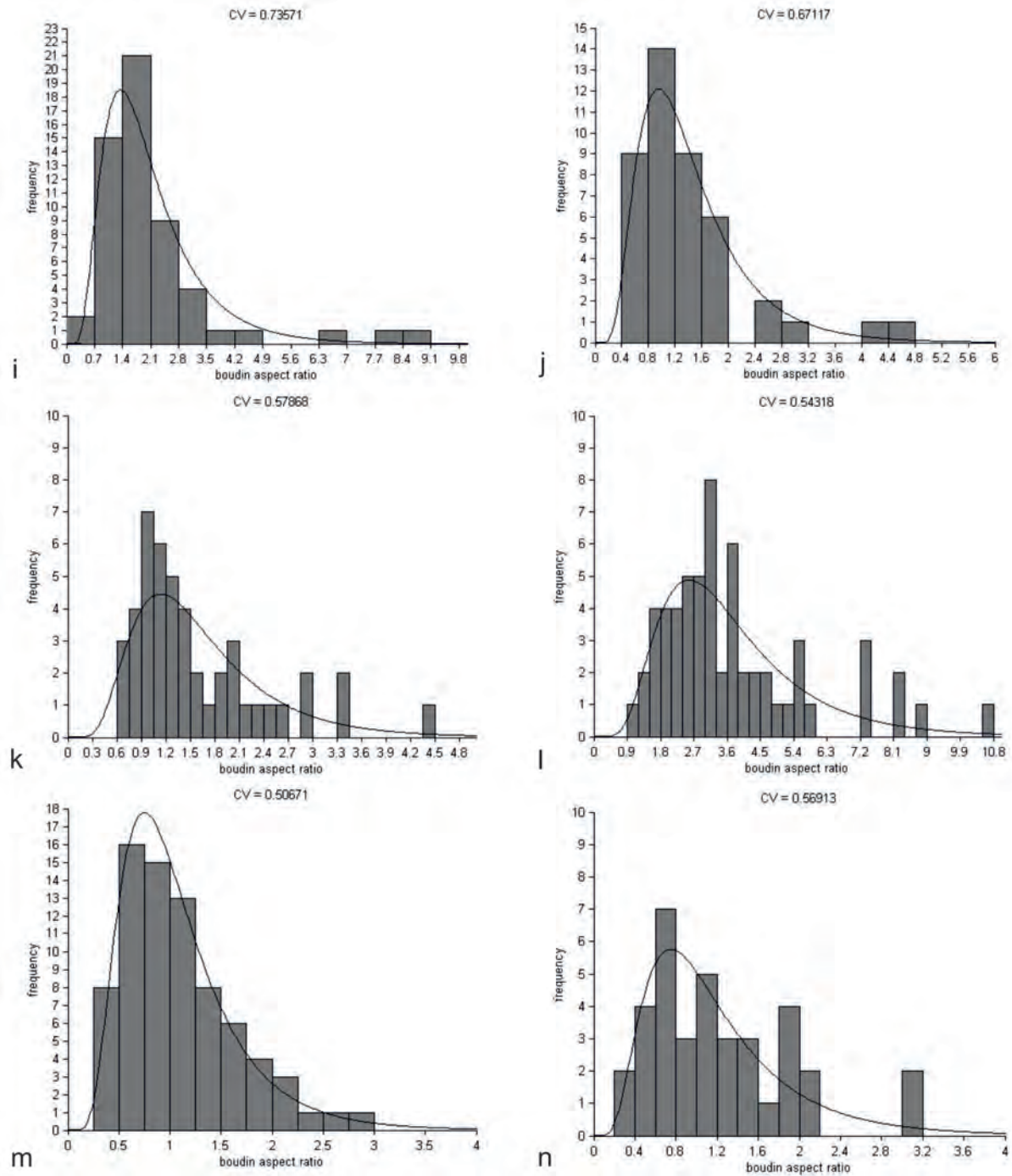
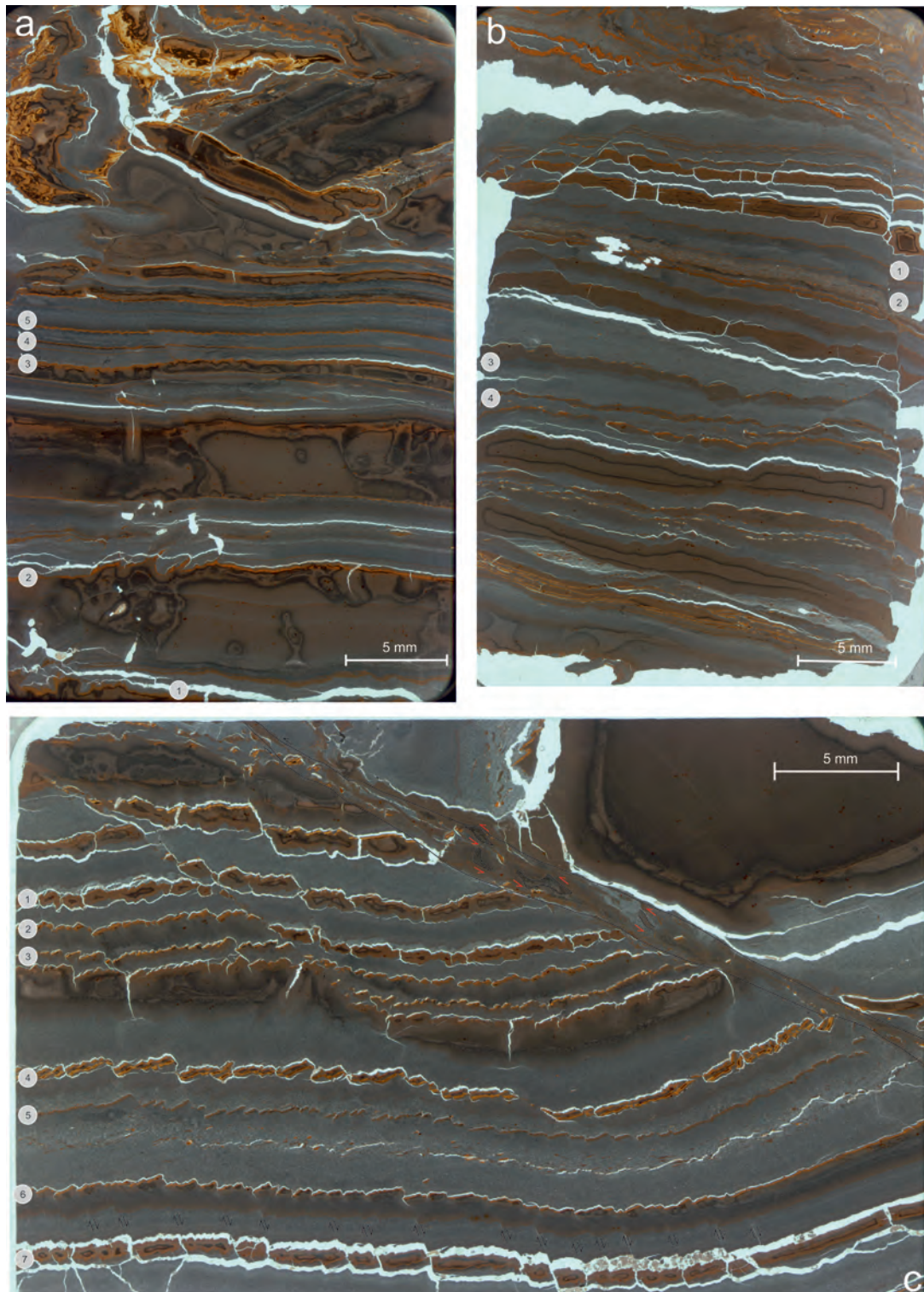


Fig. 28: Calculated aspect ratio and Coefficient of Variation: a) Layer 3 from Fig. 29 a. b) Layer 4 from Fig. 29 a. c) Layer 5 from Fig. 29a. d) Layer 1 from Fig. 29b. e) Layer 2 from Fig. 29b. f) Layer 3 from Fig. 29b. g) Layer 4 from Fig. 29b. h) Layer 1 from Fig. 29c. i) Layer 2 from Fig. 29c. j) Layer 3 from Fig. 29c. k) Layer 4 from Fig. 29c. l) Layer 5 from Fig. 29c. m) Layer 6 from Fig. 29c. n) Layer 7 from Fig. 29c.



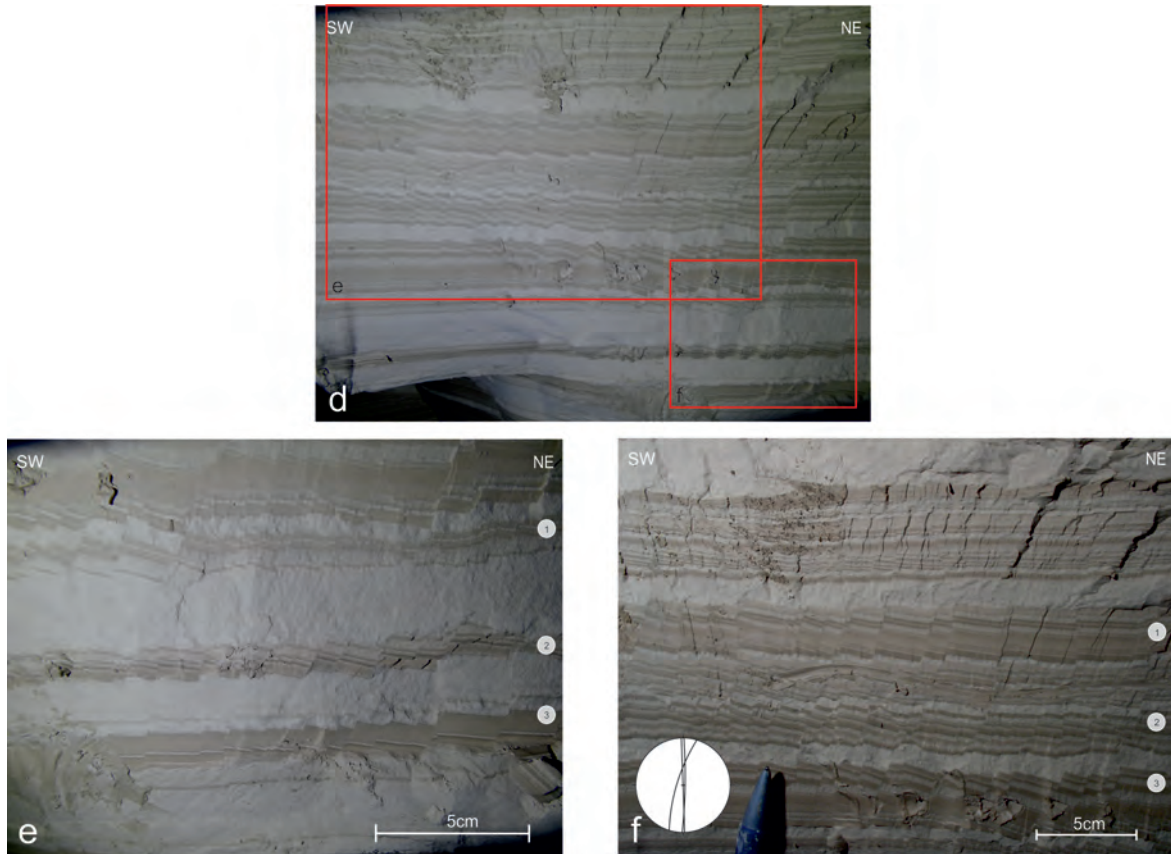


Fig. 29: Domino Boudins separated by extensional small scale faults a-c) Domino Boudins under the transmitted light microscope: a) singel layers displaying around 23.6 % extension. b) singel layers dispalying around 30.7% extension. c)singel layers display around 23.4% extension. d) dipping towards SSE and SSW, respectively, Photo by B. Grasemann. e) singel layers displaying around 8.6 % extension, Photo by B. Grasemann. f) singel layers dispalying around 8.7% extension, Photo by B. Grasemann.

A look to Fig. 27 also shows a log normal distribution of aspect ratios and that most values are smaller than one, meaning that the boudins are thicker than long. Layers show Variation Coefficient (CV) ranging between 0.70 and 0.48 , and Polarities from 1.0 to 0.65. The CV tells us that in that particular case, single faults separting the boudins do not cluster significantly due to the fact they are smaller than one. Polarities indicate that most of the faults and in some sampelline (Fig. 29e_3 and Fig. 29f_1) even all the faults are dipping to the left in our case to the SW. The different investigated sampellines display extension of at least 4.63 % to a maximum of 13.04 % extension.

The darker layers seem to behave in a more brittle way than the brighter ones, as the faults can be easier traced in the dark layers and they also show a clear offset. Plot shows that the small scale faults are dipping steeply SSE and SSW. The aperture angel α varies in the described domino boudins sets between 145.02° and 65.63° with a mean aperture angel of around 100° and a mean rotational angle Θ of 16.7° . The aperture angle α implies the initial inclination between horizontal layers and the fault. After the initiation of the brittle behavior the boudins rotated along their own axes with the rotational angle Θ . Thinsections shown in Fig. 29 a-c, are unoriented samples, therefore no preferred dip-direction and slumping-direction can be assumed. Considering the polarity the dip direction is only preferring one direction whether to the left or to the right.

The following 14 sample lines were chosen to represent the microscopical observation and measurements of the structural features. In total within the represented sample lines 675 single boudins have been measured. Their length ranges from 2.15 mm to a minimum of 0.05 mm with an average length of 0.50 mm and an average thickness of 0.35 mm. The minimal observed thickness is 0.1 mm and an maximal thickness was observed with 0.7 mm. That leads to aspect ratios between 15.36 and 0.09, whereat the mean is 1.39, showing that the boudins are rectangular and display an log normal distribution (Fig. 28).

Furthermore layers show CVs' from 0.78 to 0.44 and implies that faults separating the boudins do not cluster significantly as their values are smaller than 1. In regard to the Polarity values are ranging from -0.87 to -1. Expressing that almost all respectively in some sampellines all faults are dipping towards the right. Once more it should be mentioned that measurements were taken on unoriented samples and that the dip-direction of the faults within the thinsection is not a significant statement. Extension amounts from 50.8 % to 8.7 %. The average aperture angle α is about 120° with a maximum α of 212.36° and a minimum aperture angle of 10.52° . The average boudin measured in the thinsection rotated around 23° the measured rotational angle Θ ranges from 1.58° to 81.92° . Once more the brittle behavior of the boudins can be easier traced in the clay-enriched, fine grained, darker sections.

Length and thickness in field data and microscopic observation differ in one magnitude of their size. Although aspect ratios in microscopic measurements and in field data show a log-normal distribution, the ones in microscopic-scale are significantly larger Fig. 30. Meaning that the boudins in the thinsections are proportional longer and thinner than those observed in the field. Polarity differs only in their dip-direction but hardly in their mean values. Almost all of the fault sets dip in a preferred orientation. Coefficient of Variation (CV) shows a slightly wider spread in the outcrop data than in the microscopic valuations and imply that some sampelline in the field observations cluster more than the measurements in microscopic-scale. Within the microscopic fault sets a much higher extensional rate have been evaluated as well as a bigger aperture angle α and a slightly higher rotational angle Θ . The bigger aperture angle α indicates, that the smaller- scaled faults do have a shallower dip-angle than the bigger faults in the field.

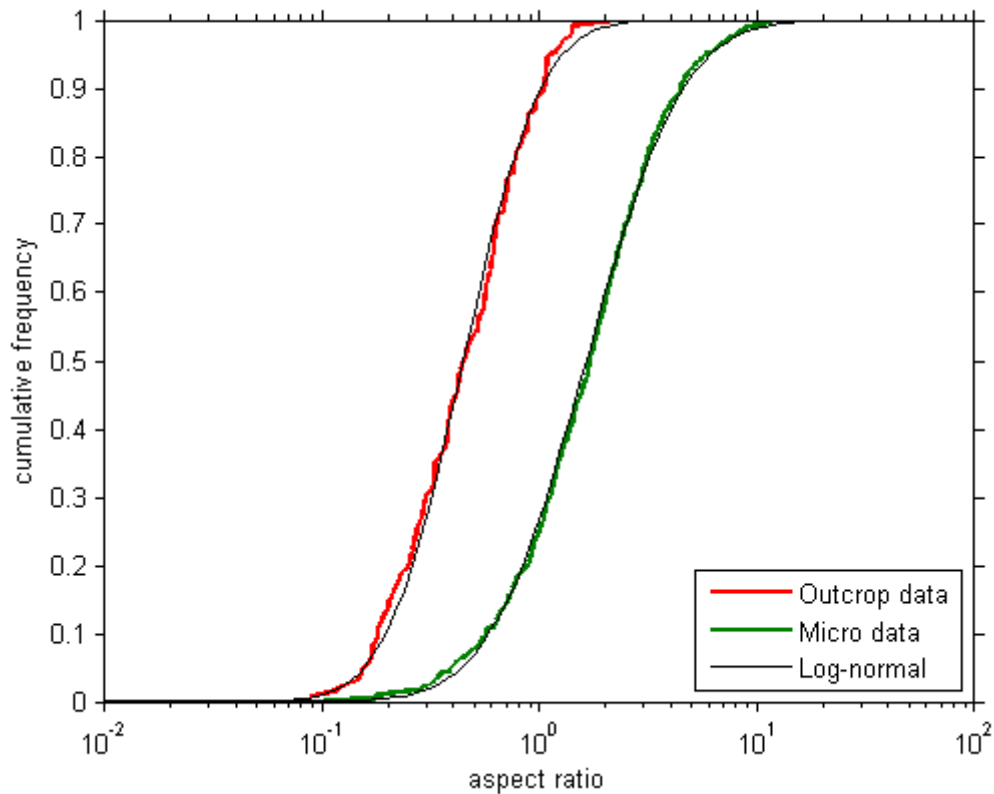


Fig. 30: Cumulative frequency plot of aspect ratios.

Tab. 1: Tabel of relevant taken measurements.

	Length [mm]				Thickness [mm]	Aspect Ratio				Polarity	CV	Extension [%]	Aperture Angle α [°]				Rotational Angle Θ [°]				N
	Max.	Min.	Mean	Median		Max.	Min.	Mean	Median				Max.	Min.	Mean	Median	Max.	Min.	Mean	Median	
Fig. 25b_1	15.48	1.66	5.27	4.51	11	1.41	0.15	0.48	0.41	0.89	0.64	11.36	121.74	65.63	10.37	101.80	61.62	1.62	19.02	18.85	32
Fig. 25b_2	12.58	1.46	6.16	5.73	10	1.26	0.15	0.62	0.57	0.65	0.58	13.04	142.142 was 63	83.12	102.53	98.17	60.62	2.77	21.12	16.66	24
Fig. 25b_3	22.84	1.15	7.37	6.53	10	2.28	0.12	0.74	0.65	1.00	0.70	6.16	113.77	86.64	99.19	100.09	90.38	3.37	15.14	10.42	16
Fig. 25c_1	36.73	3.20	16.52	15.52	26	1.41	0.12	0.64	0.60	1.00	0.61	13.15	119.19	83.45	100.66	98.48	553.54	2.80	12.36	9.11	13
Fig. 25c_2	27.78	1.74	10.19	10.32	20	1.39	0.09	0.51	0.52	0.89	0.55	4.63	145.02	81.49	104.40	98.33	62.83	3.17	14.61	9.59	23
Fig. 25c_3	25.61	5.16	12.79	11.16	34	0.75	0.15	0.38	0.33	0.81	0.48	8.25	115.60	90.00	101.50	98.63	42.83	8.20	17.82	18.51	21
Fig. 26d_3	0.88	0.11	0.36	0.36	0.4	2.21	0.28	0.90	0.90	-0.92	0.48	29.12	155.25	97.14	126.82	127.21	36.04	6.28	17.71	15.90	57
Fig. 26d_4	1.54	0.10	0.31	0.28	0.1	15.36	0.98	3.11	2.78	-0.87	0.62	25.16	156.02	92.69	130.90	131.95	27.44	3.14	14.06	13.59	63
Fig. 26d_5	1.24	0.08	0.31	0.24	0.1	12.45	0.76	3.07	2.45	-0.90	0.69	16.62	161.90	82.23	122.24	123.43	36.55	1.90	14.62	13.16	62
Fig. 26e_1	1.35	0.05	0.40	0.29	0.5	2.70	0.10	0.79	0.57	-0.98	0.78	31.42	155.56	81.77	133.86	137.00	38.17	4.20	16.37	14.86	42
Fig. 26e_2	1.31	0.08	0.35	0.28	0.3	4.38	0.25	1.16	0.92	-0.90	0.63	33.24	159.98	98.34	130.63	132.23	45.03	5.19	21.36	20.34	50
Fig. 26e_3	1.31	0.16	0.60	0.56	0.5	2.64	0.32	1.21	1.11	-0.91	0.44	33.79	144.26	13.89	118.83	122.08	56.48	7.65	19.55	15.30	21
Fig. 26e_4	1.20	0.09	0.48	0.42	0.3	4.00	0.32	1.59	1.41	-1.00	0.53	24.35	158.69	94.00	127.04	126.01	99.27	6.38	23.33	18.86	26
Fig. 26f_1	1.52	0.09	0.65	0.60	0.5	3.04	0.17	1.3	1.19	-1.00	0.55	34.21	212.36	69.36	116.60	113.67	60.00	5.72	26.93	25.57	35
Fig. 26f_2	1.77	0.11	0.43	0.36	0.2	8.87	0.57	2.13	1.77	-0.99	0.74	59.80	156.94	10.52	114.54	115.06	64.45	8.62	29.95	26.72	56
Fig. 26f_3	1.93	0.22	0.59	0.48	0.4	4.83	0.55	1.47	1.19	-1.00	0.67	13.43	145.13	37.52	110.69	113.74	68.69	2.32	28.88	26.75	44
Fig. 26f_4	1.98	0.25	0.66	0.53	0.4	4.95	0.62	1.65	1.33	-0.92	0.58	20.35	161.20	62.28	109.88	110.02	49.00	10.35	27.79	20.96	47
Fig. 26f_5	1.51	0.16	0.53	0.44	0.1	10.8	1.16	3.77	3.17	-0.94	0.54	-	139.59	60.67	103.38	106.52	81.92	1.58	29.01	27.31	60
Fig. 26f_6	1.15	0.13	0.44	0.39	0.4	2.87	0.32	1.09	0.96	-1.00	0.51	-	138.58	54.23	108.77	106.60	57.55	13.88	29.18	27.53	76
Fig. 26f_7	2.15	0.27	0.84	0.75	0.7	3.07	0.39	1.20	1.07	-1.00	0.57	8.74	148.24	92.93	110.36	117.23	36.25	6.77	24.55	26.75	36

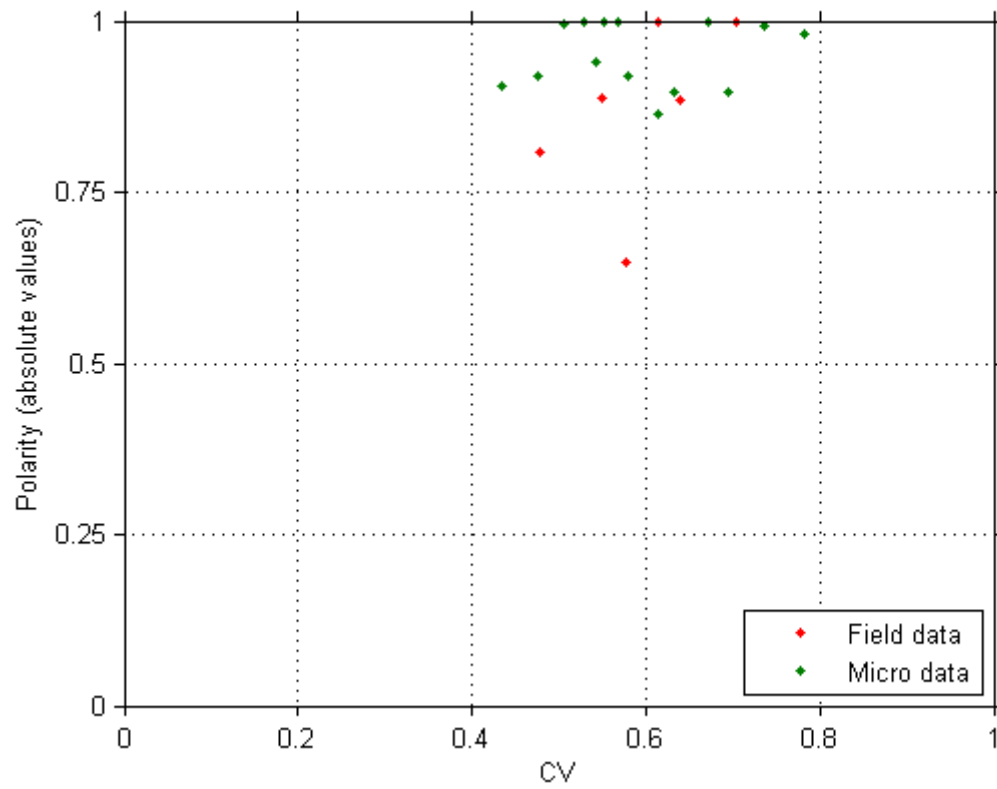


Fig. 31: Scatters plot of Coefficient of Variation (CV) and absolute values of Polarity.

DISCUSSION

6.1 POTENTIAL SOURCE OF SEISMIC EVENTS

Minor seismicity recorded along the ENE-striking Salzach-Ennstal-Mariazell-Puchberg (SEMP) sinistral strike slip fault, prove recent fault activity and might be a possible seismogenic source (Rosenberg & Schneider, 2008). The SEMP is the major strike slip fault in the Eastern European Alps (Frost *et al.* (2009); Hausegger & Kurz (2013); Linzer *et al.* (2002)). On a length of approximately 400 km from the Tauern Window through the Northern Calcareous Alps (NCA) to the Vienna Basin the fault accommodates with ~ 60 km offset the active extrusion of the Eastern Alps towards the Pannonian Basin. (Plan *et al.*, 2010) (Linzer *et al.*, 2002) The Hirlatzhöhle is located on the Ennstal segment of the SEMP. The main tectonic activity of the SEMP dates back to Oligocene and Miocene time (Rosenberg & Schneider, 2008). It was activated during collision of the Adriatic and the European plate, either as a result of lateral extrusion in east direction or by oblique indentation of the South Alpine block (Cole *et al.*, 2007). The fault lies approximately 15 km south of the outcrop in the Lehmklamm. Right above the outcrop wall a fault within limestone, which might be connected to the SEMP, was found. The fault on the ceiling is steeply dipping towards the SW (252/80) (Fig. 32). Distance between ceiling and outcrop wall amounts up to 1 m.

Within the last years (1998-2013) in the near vicinity and along the SEMP several macroseismic events with intensities between 2 and 5 behanced (Tab.2). Compared to the Environmental Seismic Intensity Scale 2007 (ESI 07, International Union of Quaternary Research INQUA)) for creating soft sediment deformation in fine grained sediments, due to liquefaction, with amplitudes up to 3 cm intensities with at least IV are needed. The observed fault on the ceiling, the SEMP and recent recorded minor seismic activity in the region are obvious mechanism to trigger soft sediment deformation within the Lehmklamm (Fig. 33).

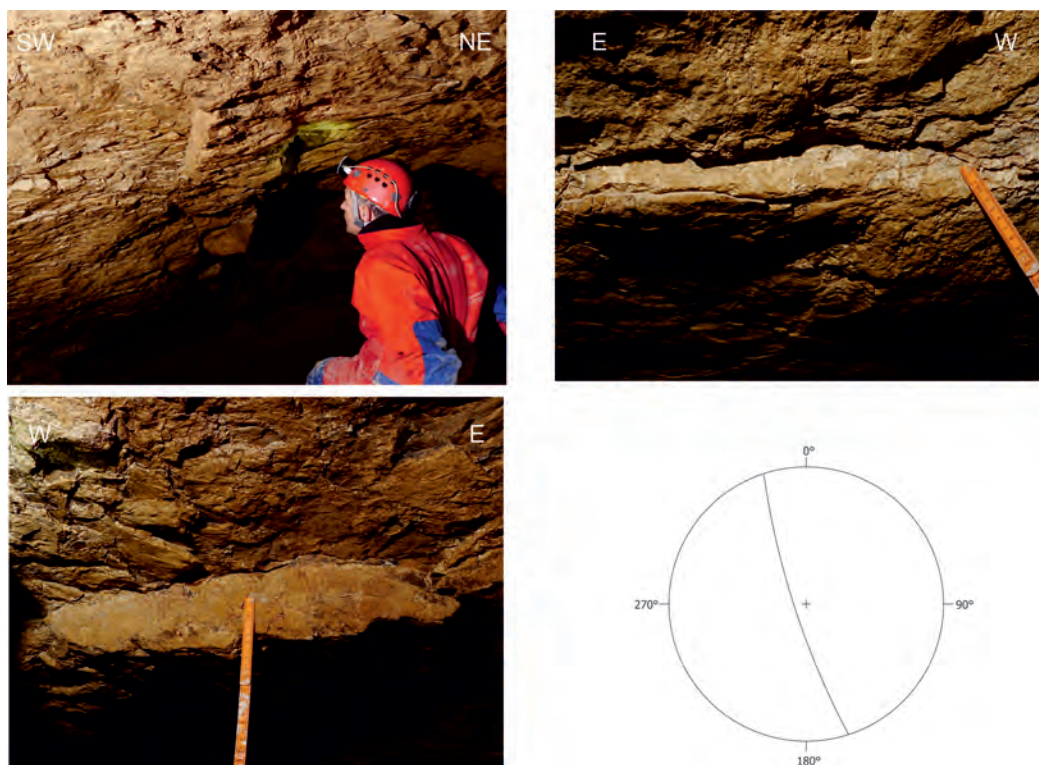


Fig. 32: Steep SW dipping fault in Carbonate right above the outcrop (252/80) ; max distance to outcrop wall 1 m, min distance 0.12 m, Photos by L. Plan.

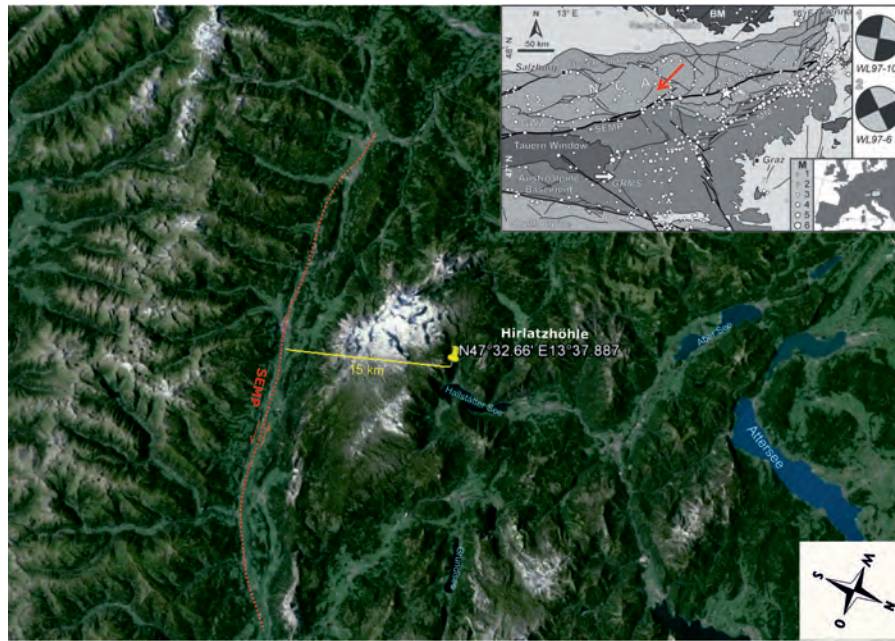


Fig. 33: SEMP ENE-striking active fault. Active tectonic map of the Eastern Alps after Reinecker and Lenhardt, 1999 (Reinecker & Lenhardt (1999)).

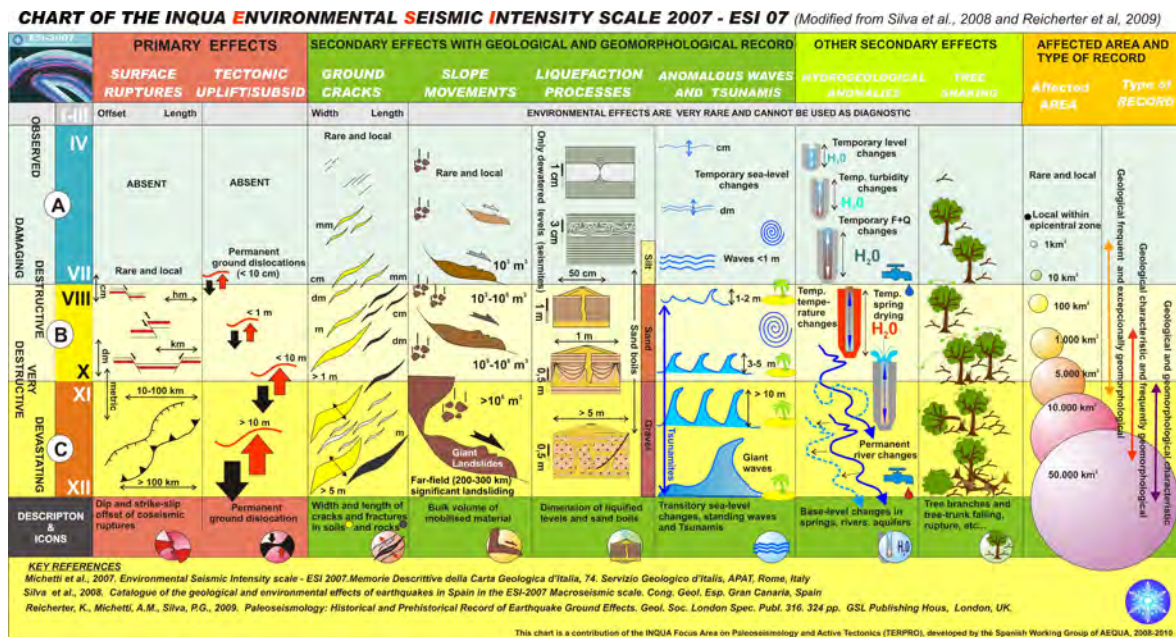


Fig. 34: ESI Chart

6.2 INTERPRETATION OF SEDIMENTOLOGICAL INVESTIGATIONS

Heavy mineral analysis (Fig. 19) of four samples leads to the assumption, that the source is an amphibolite facies rock with greenschist facies overprint. The source rock might most probably originates south from the Austroalpine Crystalline. The NCA are characterized by paleosurfaces formed in the Late Eocene Frisch (2003) to Early Oligocene. During Oligocene time, the Dachstein paleosurface subsided and was sealed with the Augenstein Formation (terrestrial conglomerates and sandstones). Their source area is considered to be predominantly of weak metamorphic terrains, such as the Greywacke Zone and equivalents, as well

Epicentrum	Date	I_0	M_L	D (km)
Wagrain	19.02.1998	IV	3.0	35
Wagrain	19.02.1998	IV	3.3	35
NW from Liezen	23.07.1998	IV	3.1	45
Gams bei Hieflau	02.04.1999	IV	2.3	87
St.Martin/Grimming	10.11.2001	IV	2.4	27
St.Martin/Grimming	10.11.2001	III	2.1	27
Bad Goisern	14.07.2003	IV	2.9	10
Hallstatt	22.02.2004	IV	2.4	2
Hallstatt	12.04.2004	IV	0.7	2
Bad Aussee	08.05.2004	III-IV	1.5	13
W of Weichselboden	28.03.2004	IV	2.4	116
Obertraun	23.06.2005	IV	1.9	4
Altaussee	22.05.2006	IV	3	14
Hallstatt	22.08.2006	III	2.3	2
Bad Ischl	15.12.2006	III-IV	2.9	18
Liezen	16.03.2008	IV	2.5	45
Hallstatt	03.05.2008	(IV)	2.5	2
Dachstein	21.05.2008	(III-IV)	3	10
Dachstein	21.05.2008	(IV)	3.6	10
E of Dachstein	18.07.2008	V	3.8	10
Altaussee	19.01.2010	II-III	2.7	14
Gosaukamm	04.08.2010	IV-V	3.3	11
Gosaukamm	05.08.2010	III-IV	2.7	11
Bad Ischl	23.10.2010	III-IV	2.4	18
Altaussee	05.04.2011	IV	3.1	14
Altaussee	10.08.2011	III	2	14
Bad Ischl	13.05.2012	IV-V	2.5	18
Bad Ischl	13.05.2012	V	2.8	18
8 km E of Admont	20.01.2013	IV	2.1	70
Hieflau	17.09.2013	II-III	1.5	84

Tab. 2: Recorded macroseismic earthquakes from 1998- 2013 along the SEMP near the Hirlatzcave and vicinity (ZAMG). I_0 ... intensity, M_L ...local magnitude D...distance.

as siliciclastics to the south of the depositional area. Sedimentation was terminated in the Early Miocene, caused by the collapse of the Eastern Alps and the surfaces were denuded. Afterward the Dachstein surface experienced uplift in several pulses. The Augenstein formation is only preserved in areas where karstic erosion occurs.

With cognition of the mineralogical bulk composition (Fig. 17) and heavy-mineral analysis (Fig. 18) couplets of brighter and darker deposits are regarded as fluvio-lacustrine, annual varve-like deposits. Clay mineralogy reveals that illite, smectite, kaolinite and chlorite are more abundant in the darker layers. The higher amounts of kaolinite and expandable smectite and the absence of K-feldspar in the darker layers could indicate increased chemical weathering caused by seasonal variations. The brighter layers are enriched in carbonates. The darker clastic-rich layers are considered to be the summer de-

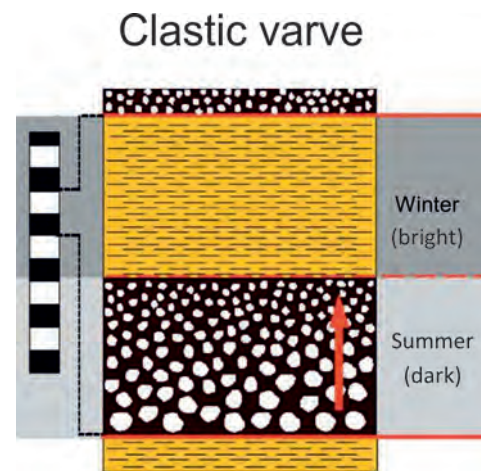


Fig. 35: Model of clastic varve formation. Design: Sturm M. and Lotter A. (1995) Lake sediments as environment archives. EAWAG News 38E: 6-9 (Zolitschka, 2007).

posits, while the quartz- and carbonate enriched layers are assumed to have been deposited during the winter months (Fig. 35).

6.3 ESTIMATION OF PERIODICITY

Couplets of the fluvi-lacustrine deposits forms rhythmic varve-like layer-cake. Single layers in between two deformed strata were counted to compute the relative time in between seismic events. Due to the assumption that layers were sedimented in annual varves, the total counted number of beds were divided by two to convert them into years. Additionally measurements of deposit thickness in between those seismic deformed strata were necessary to calculate the deposition in mm per year. Computed values for deposits per year ranges from 5.99mm to 1.67mm. Extrapolated on the whole outcrop wall it gives a duration of deposition between a minimum of 300 and a maximum of 1793 years. Calculated years in between periodic occurrence of earthquakes with relevant intensities ($\geq IV$) ranges between 15 and 48.5 years. Considered to more observed deformed layers in the younger part of the outcrop wall assumes a higher frequency.

1) Fig. 29f				2) Fig. 29e				3) Fig. 22d				4) Thinsections			
N_L	$\triangle a$	D [mm]	D/a [mm]	N_L	$\triangle a$	D [mm]	D/a [mm]	N_L	$\triangle a$	D [mm]	D/a [mm]	N_L	$\triangle a$	(D) [mm]	D/a [mm]
70	35	208.82	5.99	95	47.5	255.82	5.39	97	48.5	159.21	3.28	30	15	25.1	1.67
		Height of outcrop [mm]	1) \triangle Years	2) \triangle Years	3) \triangle Years	4) \triangle Years									
SW		3000	500	557	914	1793									
middle		2352	392	437	716	1406									
NE		1800	300	334	548	1076									

Tab. 3: Measurements and calculations to estimate the time in between seismic events and time needed to deposit the stratas; N_L ...Number of layers, a ...years, D ...deposits, D/a ...deposits per year.

6.4 STRUCTURAL INTERPRETATION

Structures are assumed to have been triggered by cyclic seismic event under highly water saturated conditions near the water-sediment surface, as they are observed inbedded between undeformed strata (Fig. 37). Rapid sedimentation might trap water increase the pore fluid pressure and enhance dramatically the chance to undergo gravitational slumping. The varve-like sediments in the Lehmklamm show a relative stable lateral layerthickness and are therefore not likely to undergo gravitational gliding due to sediment overload.

Formation of structures occur due to (i) pore fluid overpressure and resulting liquefaction and (ii) N-directed gravitational gliding (Fig. 36). Slickenside on the SW end of the outcrop wall suggests north directed gravitational slumping (Fault plane SS 340/04, Linear 359/02).

Differences in the proportional length and thickness of boudins measured in thinsections and outcrop scale (Fig. 30) might follow from truncation. At small scale, such as in thinsections, truncations are known as left-hand truncation (LHT). They are usually related to measurement method. In regard to measured length of boudins in thinsection, the graphical resolution might be limited. Meaning that not every single small scale fault separating the boudins might be measured, resulting in a loss of data and in larger aspect ratios. Also known as LHT "fall-off". (Pickering *et al.*, 1995)



Fig. 36: Slickensides (SS 340/04, LS 359/02) indicating north directed gravitational slumping.

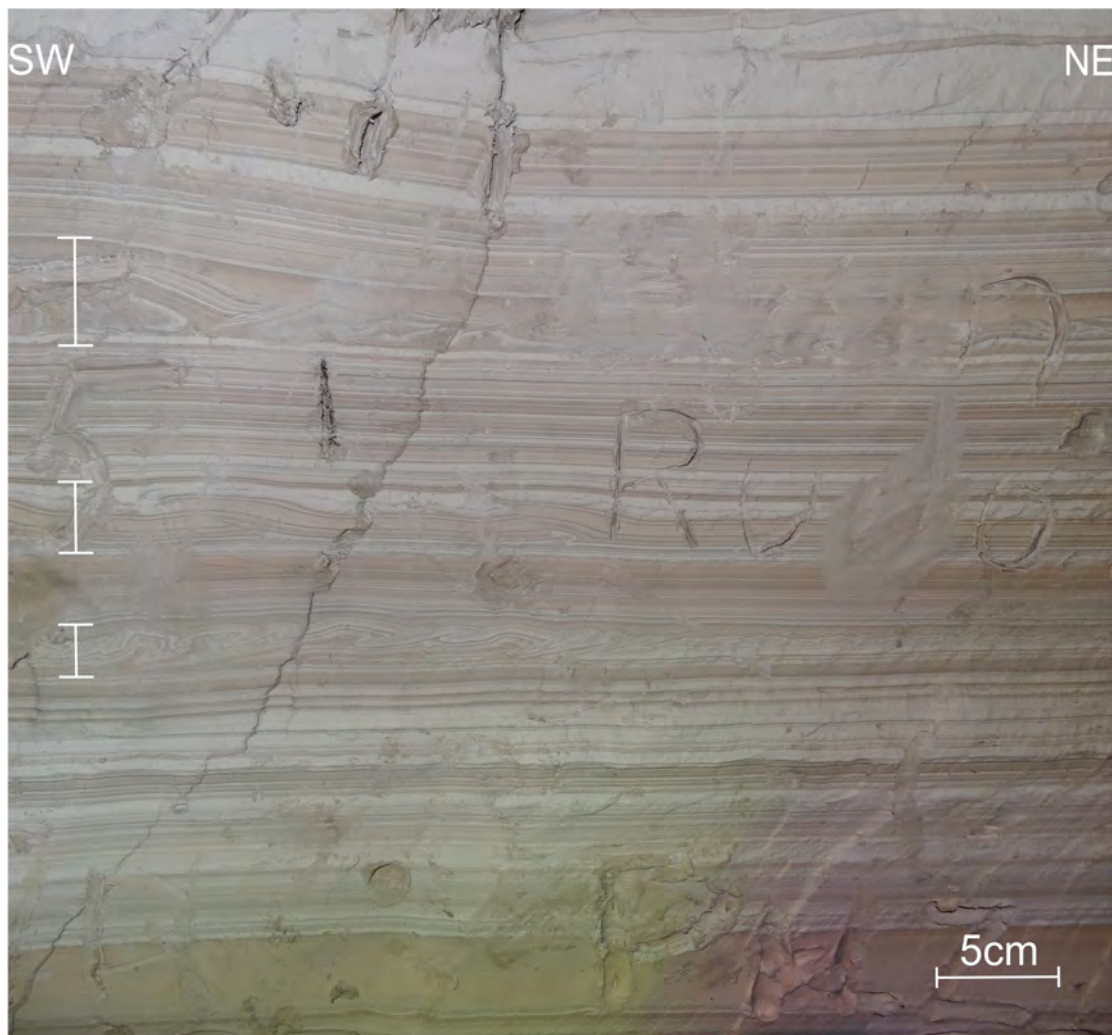


Fig. 37: Deformed strata inbedded between undeformed ones are interpreted as cyclic seismogenic activity.

CONCLUSION

In summary the investigated soft-sediment structures in the Hirlatz cave were triggered

- (i) by periodic seismic events: Deformed slumped units are separated from each other by undeformed strata and give a clear evidence of being triggered by several seismic events.
- (ii) under highly water saturated conditions: Earthquake shaking increases the pore fluid pressure and resulting in liquefaction within the cm- varved sediments leading to a loss of cohesive strength and initiate a single point failure. Subsequently liquefaction decreases the shear strength and leads to density discontinuities making N- directed gravitational gliding and formation of the observed structures more favorable.
- (iii) at or close to the water-sediment interface: Seismogenic shaking only affects the upper most cm of the water saturated sediments. Horizontal stratified sediments provide an easy-slip zone, building a basal detachment zone along which deformation is initiated.
- (iv) by earthquakes with a minimum intensity of IV: Earthquakes with a minimum intensity of IV must have occurred periodically every 15- 48.5 years to trigger the observed structures within the fine grained, water saturated sediments.
- (v) by earthquake activities sourcing in the Salzach-Ennstal-Mariazell-Puchberg (SEMP) sinistral strike slip fault, with a maximum displacement of > 60 km about 15 km south of the outcrop which is accommodating the active extrusion of the Eastern Alps.

Sedimentological investigations under the XRD and heavy mineral analysis of the unconsolidated sediments let assume that

- (vi) Couplets of darker clastic rich summer deposits and brighter carbonate enriched winter deposits are assumed to be annual deposits. Which have been deposited under fluvio-lacustrine conditions in the Lehmklamm.
- (vii) The finely laminated clastic sediments in the Lehmklamm derive south from the Austroalpine Crystalline. Source rock originates from an amphibolite facies terrain.

Applied quantitative techniques, such as the reconstruction of the aspect ratios of boudins, the fault system polarity, the coefficient of variation of faults and kinematic balancing of field observation and unoriented samples from thinsections show

- (viii) Aspect ratios with an log- normal distribution, meaning that all boudins are rectangular. Length and thickness in field data and microscopic observation differ in one magnitude of their size. Boudins in microscopic-scale are significantly larger, implying that they are proportionally longer and thinner than those observed in the field.
- (ix) Polarity that aims that almost all fault sets dip in a preferred direction.
- (x) Coefficient of Variation (CV) indicates that the faults separating the boudins do not show significant clustering. Slightly greater spreading in the outcrop data than in the microscopic valuations imply that some sampellines in the field cluster more than the measurements in microscopic-scale.
- (xi) Within the microscopic fault sets a much higher extensional rate has been evaluated as well as a bigger aperture angle α and a slightly higher rotational angle Θ . A bigger aperture angle α indicates, that the smaller- scaled faults do have a shallower dip-angle than the bigger faults in the field.

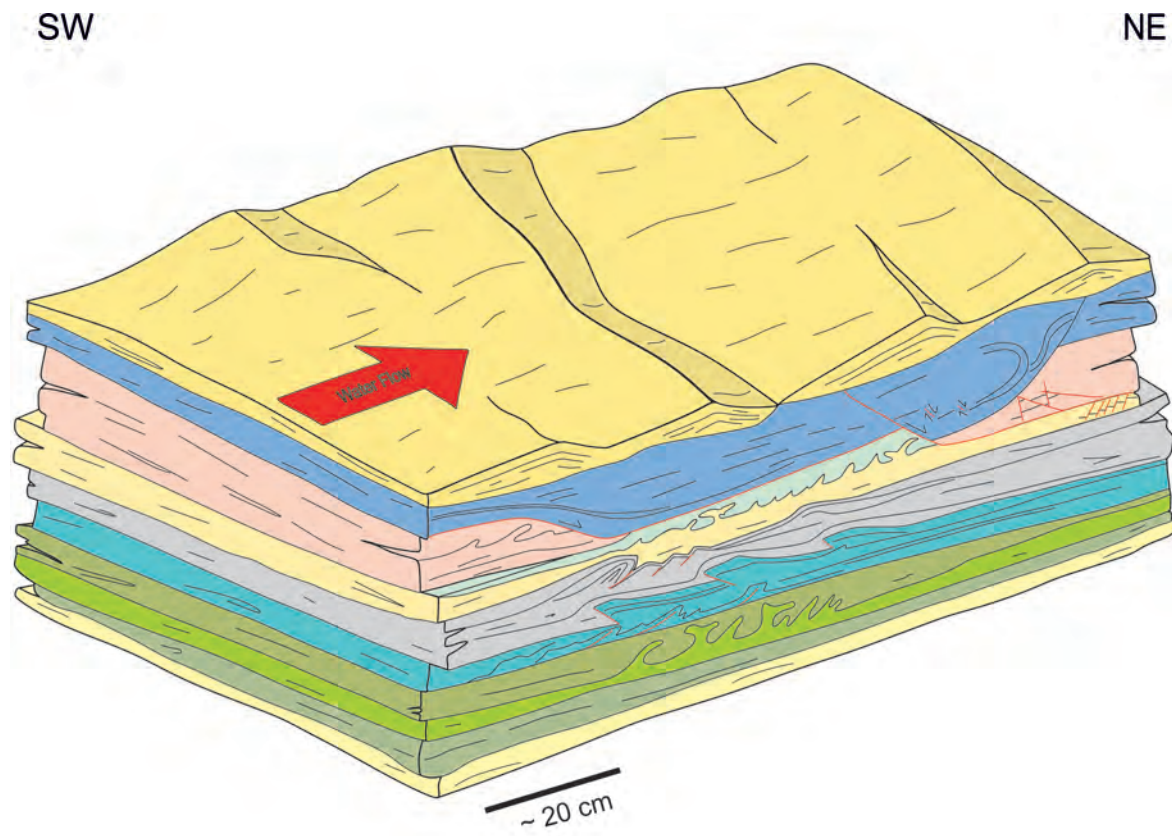


Fig. 38: Simplified graphical representation of the outcrop

ACKNOWLEDGMENT

I want to express my warm thanks to my supervisors Prof. Dr. Bernhard Grasemann and Mag. Dr. Lukas Plan. Most of all I want to thank them for their understanding, motivation and mentoring at any time and stage of my thesis. I would also like to thank Prof. Mag. Dr. Susanne Gier for her guidance and support with sedimentological problems and encouraging words at the beginning of writing my thesis. A big thank goes to Mag. PhD Martin Schöpfer without his support I still would be trying to fix problems in MatLab. I also want to thank him, for the time and patience he invested in helping me. Furthermore I want to express my acknowledgment to Dr. A. Hugh N. Rice for his advice and Andreas Wagner for the preparation of the thin sections and Dr. Benjamin Huet. For a helping hand with all kind of difficulties, for the discussions and the enrichment of my time at University of Vienna I want to thank my colleagues and dear friends, Romana Gritzmann, Dominik Reichartzeder, Gregor Ortner, Gregor Dober, Katharina Böhm, Chloé Asmar, Maria Michail, Franziska Mayerhofer, Christopher Kollmann, Karoline Lindner, Hagen Bender, Maarten Voorn and Andreas Gerner. My time at University and the field trips would not have been the same without them. Thank you for the good time we had together and helping me shaping my personality. I want to express my gratitude towards my family, for supporting and encouraging me all the time and giving me the possibility for living my dreams and enable my education. Thank you Julian Salomon and Gottfried Salomon for living and showing us strength and purposefulness with a healthy portion of joie de vivre.

LIST OF FIGURES

Figure 1	Tectonic map of the Alps, Schuster <i>et al.</i> (2010) after Schmid <i>et al.</i> (2004).	7
Figure 2	Tracing paths in the western part of the Dachsteinmassif Pohl & Greger (2001).	9
Figure 3	Large-scale paleogeographic reconstruction for (a) Late Triassic, (b) Late Jurassic and (c) Late Cretaceous times. G: Genève; W: Wien Schmid <i>et al.</i> (2004).	10
Figure 4	Stratigraphy of Dachstein-nappe after Buchegger & Greger (1998).	10
Figure 5	Lofer Zyklthem, singel bed out of the Dachsteinkalk, cyclic sedimentation shows variation of the sealevel after Faupl (2003).	11
Figure 6	Simplified cross-section through the Dachstein-massif based on ÖK 96 u. 127 and geological map of the Dachstein region Mandl (1998) drawn by Robert Seebacher (Seebacher, 2006).	11
Figure 7	Depth of liquefaction, affected by depth below surface and seismic shear stress. C, number and shaking cycles Seed, H.B., Idriss (1971).	12
Figure 8	Geometric analogies from the Dead Sea Basin Alsop & Marco (2011)	14
Figure 9	(a) fine-grained varved deposition. (b) seismic triggered soft-sediment deformation caused by liquefaction in the uppermost highly water saturated layers (c) continuous sedimentation after Becker <i>et al.</i> (2006).	14
Figure 10	Atterberg cylinder.	15
Figure 11	Bragg's law; λ ...wavelength; d ...lattice plane distance; Θ ...incidence angle; n ...integer.	16
Figure 12	Apparatus for heavy mineral separation A. funnel with heavy liquid tetrabromethane B. rubber sleeve and pinch cock C. funnel and filter paper D. collecting tray.	17
Figure 13	Fault system polarity shows values from -1 to 1, $P=-1$ all faults dipping to the right $P=0$ amount of left and right dipping faults equal distributed $P=1$ faults dipping to the left.	17
Figure 14	Parameter to quantify Domino-boudins: L...length W...width D...offset α ...aperture angle Θ ...rotational angle.	18
Figure 15	Fault system polarity: D...displacement fault dipping towards the right -D...displacement fault dipping towards the left T...throw H...heave.	18
Figure 16	Coefficient of variation, where $CV < 1$ do not cluster and $CV > 1$ do cluster.	18
Figure 17	Bulk mineralogy; X-ray diffraction patterns: HI 9...middle brown clay-sized layer, HI 8...dark clay-sized layer, HI 7...bright clay-sized layer, HI 6...calcareous cover, HI 4...coarser grained (maybe Augenstein) from top, HI 3... fine grained sandy sample from current ripple, HI 2... fine grained sand detachment zone.	19
Figure 18	Clay mineral analysis: Samples were treated in 5 different ways to distinguish different clay minerals. blue graph with MgGly...Magnesium Glycerin, purpel saturated with Mg...Magnesium, green with KT...Kalium and temperd at 550 °C, black with KEG...Kalium Ethylenglycol, red with K1...simply saturated with Kalium. a) shows sample HI 7. b) graphs of sample HI 8. c) X-ray diagram of sample HI 9. d) comparison of samples HI 9, HI 8 and HI 7.	20
Figure 19	Heavy mineral analysis: a) HI 3... fine grained sandy sample from current ripple. b) HI 2... fine grained sand detachment zone c and d) HI 4...coarser grained (maybe Augenstein) from a depression at the top of the outcrop wall.	21

- Figure 20 a) current ripple indicating north directed paleo flow; Photo by L. Plan b) actual current with south directed flow; Photo by Lukas Plan c) current ripple: north-wards flow; Photo by L. Plan d) duplex with steep SW dipping axial plane (300/85) and gently NE dipping fold axes (023/05); Photo by B. Grasemann. 22
- Figure 21 Kelvin-Helmholtz Instabilities in clouds, conspicuous analogies to sedimentary flame structures Kaushik (2013). 22
- Figure 22 a) intruded cusps representing 22.2 % shortening, Photo by L. Plan b) flame structures c) fishtail and flame structures with cusps and turbulent structures accomadating 54.5 % shortening, Photo by B. Grasemann d) intruded flames 46.8 % shortening, Photo by L. Plan e) structures c, and d, occuring in one stratigraphic level, Photo by L. Plan. 23
- Figure 23 Conspicuous analogies in mm-scale to observation in 24, unoriented sample. 24
- Figure 24 Erosive base (Grey) and two generartions of listric faults, younger fault (red) cuts through the older fault (green) moderataly dipping towards the N and NE, respectively; slumping fold generated during activation of green listirc fault, fold plane dipping moderatley towards the SE, Photo by L. Plan. 24
- Figure 25 Development of slump systems after Alsop & Marco (2011). Not the full range of phases are observed. 25
- Figure 26 Examples of slump folds. a) and b) slump fold generated during early phase of gravitational down-slope movement. c) thrust fault, 3.8 % shortening. d) imbricated thrust faults. e) & f) thrust fold with synkinematic boudins. g) SW-directed downslope slumping, with hook fold geometries. h) NE- directed downslope verging type 3 refold patterns. i) disassociated clast with incorporated fold. j) backthrusting detachment fold with box fold like geometry. 26
- Figure 27 Calculated aspect ratio and Coefficient of Variation: a) Layer 1 from Fig. 29e. b) Layer 2 from Fig. 29 Sedimentary archives are for that reason an important access to determine the reoccurrence of paleoearthquake activity. e. c) Layer 3 from Fig. 29e. d) Layer 1 from Fig. 29f. e) Layer 2 from Fig. 29f. f) Layer 3 from Fig. 29 f. 27
- Figure 28 Calculated aspect ratio and Coefficient of Variation: a) Layer 3 from Fig. 29 a. b) Layer 4 from Fig. 29 a. c) Layer 5 from Fig. 29a. d) Layer 1 from Fig. 29b. e) Layer 2 from Fig. 29b. f) Layer 3 from Fig. 29b. g) Layer 4 from Fig. 29b. h) Layer 1 from Fig. 29c. i) Layer 2 from Fig. 29c. j) Layer 3 from Fig. 29c. k) Layer 4 from Fig. 29c. l) Layer 5 from Fig. 29c. m) Layer 6 from Fig. 29c. n) Layer 7 from Fig. 29c. 29
- Figure 29 Domino Boudins separated by extensional small scale faults a-c) Domino Boudins under the transmitted light microscope: a) singel layers displaying around 23.6 % extension. b) singel layers dispalying around 30.7% extension. c) singel layers display around 23.4% extension. d) dipping towards SSE and SSW, respectively, Photo by B. Grasemann. e) singel layers displaying around 8.6 % extension, Photo by B. Grasemann. f) singel layers dispalying around 8.7% extension, Photo by B. Grasemann. 31
- Figure 30 Cumulative frequency plot of aspect ratios. 32
- Figure 31 Scatters plot of Coefficient of Variation (CV) and absolute values of Polarity. 34
- Figure 32 Steep SW dipping fault in Carbonate right above the outcrop (252/80) ; max distance to outcrop wall 1 m, min distance 0.12 m, Photos by L. Plan. 35
- Figure 33 SEMP ENE-striking active fault. Active tectonic map of the Eastern Alps after Reinecker and Lenhart, 1999 Reinecker & Lenhardt (1999). 36
- Figure 34 ESI Chart 36

-
- Figure 35 Model of clastic varve formation. Design: Sturm M. and Lotter A. (1995)
Lake sediments as environment archives. EAWAG News 38E: 6-9 (Zolitschka,
2007). 37
- Figure 36 Slickensides (SS 340/04, LS 359/02) indicating north directed gravitational
slumping. 39
- Figure 37 Deformed strata inbedded between undeformed ones are interpreted as
cyclic seismogenic activity. 39
- Figure 38 Simplified graphical representation of the outcrop 41

LIST OF TABLES

Table 1	Tabel of relevant taken measurements.	33
Table 2	Recorded macroseismic earthquakes from 1998- 2013 along the SEMP near the Hirlatzcave and vicinity (ZAMG). I_0 ... intesity, M_L ...local magnitude D...distance.	37
Table 3	Measurements and calculations to estimate the time in between seismic events and time needed to deposit the stratas; N_L ...Number of layers, a...years, D...deposits, D/a...deposits per year.	38

BIBLIOGRAPHY

- Alsop, G. I., & Marco, S. 2012a. A large-scale radial pattern of seismogenic slumping towards the Dead Sea Basin. *Journal of the Geological Society*, **169**(1), 99–110.
- Alsop, G. I., & Marco, S. 2012b. Tsunami and seiche-triggered deformation within offshore sediments. *Sedimentary Geology*, **261-262**(June), 90–107.
- Alsop, G. I., & Marco, S. 2013. Seismogenic slump folds formed by gravity-driven tectonics down a negligible subaqueous slope. *Tectonophysics*, **605**(Oct.), 48–69.
- Alsop, G.I., & Marco, S. 2011. Soft-sediment deformation within seismogenic slumps of the Dead Sea Basin. *Journal of Structural Geology*, **33**(4), 433–457.
- Becker, A. 2004. Sedimentdeformationen in der Höhle Sous-les-Sangles. 38–41.
- Becker, A., Davenport, C., Eichenberger, U., Gilli, E., Jeannin, P., & Lacave, C. 2006. Speleoseismology: A critical perspective. *Journal of Seismology*, **10**(3), 371–388.
- Becker, A., Häuselmann, Ph., & Gilli, E. 2012. Active tectonics and earthquake destructions in caves of northern and central Switzerland. *International Journal of Speleology*, **41**(January), 35–49.
- Brustur, T., & Jipa, D. C. 2007. First record of the seismites in Pliocene deposits from Prahova Valley Micro-seismicity. *Geo-Eco Marina*, **13**, 23–25.
- Buchegger, G., & Greger, W. 1998. *Die Hirlatzhöhle im Dachstein*. Hallstatt: ARGE Hirlatzhöhlenbuch.
- Cole, J., Hacker, B., Ratschbacher, L., Dolan, J., Seward, G., Frost, E., & Frank, W. 2007. Localized ductile shear below the seismogenic zone: Structural analysis of an exhumed strike-slip fault, Austrian Alps. *Journal of Geophysical Research: Solid Earth*, **112**, 1–15.
- Draganits, Erich, Grasemann, Bernhard, Janda, Christoph, Hager, Christian, & Preh, Alexander. 2014. 300MW Baspa II - India's largest private hydroelectric facility on top of a rock avalanche-dammed palaeo-lake (NW Himalaya): Regional geology, tectonic setting and seismicity. *Engineering Geology*, **169**, 14–29.
- Farrell, S. G. 1984. A dislocation model applied to slump structures, Ainsa Basin, South Central Pyrenees. *Journal of Structural Geology*, **6**, 727–736.
- Faupl, Peter. 2003. *Historische Geologie*. UTB Facultas Verlag und Buchandlung.
- Fossen, Haakon. 2012. *Structural Geology*. University of Bergen, Norway: Cambridge University Press.
- Frisch, W. 2003. Die Hochplateaus in den Kalkalpen- 35 Millionen Jahre alte Landoberflächen. *Gmunder-Geo Sutiden*, **2**.
- Frost, Erik, Dolan, James, Sammis, Charles, Hacker, Brad, Cole, Joshua, & Ratschbacher, Lothar. 2009. Progressive strain localization in a major strike-slip fault exhumed from midseismogenic depths: Structural observations from the Salzach-Ennstal- Mariazell-Puchberg fault system, Austria. *Journal of Geophysical Research: Solid Earth*, **114**, 1–14.
- Goscombe, B. D., Passchier, C. W., & Hand, M. 2004. Boudinage classification: end-member boudin types and modified boudin structures. *Journal of Structural Geology*, **26**(4), 739–763.
- Hausegger, Stefan, & Kurz, Walter. 2013. Cataclastic faults along the SEMP fault system (Eastern Alps, Austria) - A contribution to fault zone evolution, internal structure and paleo-stresses. *Tectonophysics*, **608**, 237–251.

- Heifetz, E., Agnon, A., & Marco, S. 2005. Soft sediment deformation by Kelvin Helmholtz Instability: A case from Dead Sea earthquakes. *Earth and Planetary Science Letters*, **236**(1-2), 497–504.
- Ishikawa, Masahiro, & Otsuki, Kenshiro. 1995. Effects of strain gradients on asymmetry of experimental normal fault systems. *Journal of Structural Geology*, **17**(7), 1047–1053.
- Kaushik. 2013. *No Title*.
- Kozur, H. 1991. The evolution of the Meliata-Hallstatt ocean and its significance for the early evolution of the Eastern Alps and Western Carpathians. *Palaeogeography, Palaeoclimatology, Palaeoecology*, **87**(1-4), 109–135.
- Lignier, V., & M.Desmet. 2002. Les archives sédimentaires quaternaires de la grotte sous les Sangles. *Karstologia*, **39**(1), 27–46.
- Linzer, Hans Gert, Decker, Kurt, Peresson, Herwig, Dell'Mour, Rudi, & Frisch, Wolfgang. 2002. Balancing lateral orogenic float of the Eastern Alps. *Tectonophysics*, **354**, 211–237.
- Mandl, G. 1998. Geologische Karte der Dachsteinregion, 1:50000. *Geol. Bundesanstalt, Wien*.
- Mandl, G. W. 2000. The Alpine sector of the Tethyan shelf - Examples of Triassic to Jurassic sedimentation and deformation from the. *Mitteilung Österreichischer Geologischer Gesellschaft*, **92**, 61–77.
- Marco, S., Stein, M., & Agnon, A. 1996. Dead Sea Graben Paleoseismology, JGR. *Journal of Geophysical Research*, **101**(B3), 6179–6191.
- Meyer, Michael C., Wiesmayr, G., Brauner, M., Häusler, H., & Wangda, D. 2006. Active tectonics in Eastern Lunana (NW Bhutan): Implications for the seismic and glacial hazard potential of the Bhutan Himalaya. *Tectonics*, **25**, 1–21.
- Mohindra, R., & Bagati, T.N. 1996. Seismically induced soft-sediment deformation structures (seismites) around Sumdo in the lower Spiti valley (Tethys Himalaya). *Sedimentary Geology*, **101**, 69–83.
- Moriya, Shunji, Childs, Conrad, Manzocchi, Tom, & Walsh, John J. 2005. Analysis of the relationships between strain, polarity and population slope for normal fault systems. *Journal of Structural Geology*, **27**(6), 1113–1127.
- Obermeier, S.F. 1996. Use of liquefaction-induced features for paleoseismic analysis. *Engineering Geology*, **44**(1-4), 1–76.
- Passchier, C.W., & Druguet, E. 2002. Numerical modelling of asymmetric boudinage. *Journal of Structural Geology*, **24**(11), 1789–1803.
- Pfarr, T., Seebacher, R., & Plan, L. 2014. Die längsten und tiefsten Höhlen Österreichs. *Die Höhle*, **Jg.65**(1-4), 146–150.
- Pickering, G., Bull, J.M., & Sanderson, D.J. 1995. Sampling power-law distributions. *Tectonophysics*, **248**(1-2), 1–20.
- Plan, L., Grasemann, B., Spotl, C., Decker, K., Boch, R., & Kramers, J. 2010. Neotectonic extrusion of the Eastern Alps: Constraints from U/Th dating of tectonically damaged speleothems. *Geology*, **38**(6), 483–486.
- Pohl, H., & Greger, W. 2001. Die längste Höhle Österreichs - Die Hirlatzhöhle bei Hallstatt/Dachstein/Salzkammergut. 3. *Symposium zur Geschichte der Erdwissenschaften in Österreich*, 83–84.
- Reinecker, J., & Lenhardt, W. a. 1999. Present-day stress field and deformation in eastern Austria. *International Journal of Earth Sciences*, **88**, 532–550.

- Rodríguez-Pascua, M.A. 1996. Períodos de recurrencia de paleoterremotos en sedimentos varvados lacustres del Mioveno superior. *GEOACETA*, **20**(4), 1004–1007.
- Rodríguez-Pascua, M.A., Calvo, J. P., G. De Vicente, & D. Gómez-Gras. 2000. Soft-sediment deformation structures interpreted as seismites in lacustrine sediments of the Prebetic Zone, SE Spain, and their potential use as indicators of earthquake magnitudes during the Late Miocene. *Sedimentary Geology*, **135**, 117–135.
- Rosenberg, C. L., & Schneider, S. 2008. The western termination of the SEMP Fault (eastern Alps) and its bearing on the exhumation of the Tauern Window. *Geological Society, London, Special Publications*, **298**(1), 197–218.
- Rossetti. 1999. Soft-sediment deformation structures in late Albian Âs Basin, northern Brazil: A o Luõ to Cenomanian deposits, Sa evidence for palaeoseismicity. *Sedimentary Geology*, **46**, 1065–1081.
- Sandeep, S., & Jain, A. K. 2007. Liquefaction and fluidization of lacustrine deposits from Lahaul-Spiti and Ladakh Himalaya: Geological evidences of paleoseismicity along active fault zone. *Sedimentary Geology*, **196**(1-4), 47–57.
- Schmid, S. M., Fügenschuh, B., Kissling, E., & Schuster, R. 2004. Tectonic map and overall architecture of the Alpine orogen. *Eclogae Geologicae Helvetiae*, **97**, 93–117.
- Schuster, Ralf, Kurz, Walter, Krenn, Kurt, & Fritz, Harald. 2010. Introduction to the Geology of the Eastern Alps. 121–133.
- Seebacher, R. 2006. Aktuelle Forschungen in der Südwandhöhle (Dachsteinloch, 1543 / 28), Stmk / OÖ. *Die Höhle*, **57**(1-4), 76–89.
- Seed, H.B., Idriss, I.M. 1971. Simplified procedures for evaluating soil liquefaction potential. Proceeding of American Association of Civil Engineering. *Journal of Soil Mechanics Foundation Division*, **94**, 1249–1273.
- Seilacher, A. 1969. Fault-graded beds Interpreted as Seismites. *Sedimentology*, **13**(1-2), 155–159.
- Tuttle, M. P. 2001. The use of liquefaction features in paleoseismology: Lessons learned in the New Madrid seismic zone, central United States. *Journal of Seismology*, **5**, 361–380.
- Üner, S., Ye, Ç., & Yakupo, T. 2009. *The Traces of Earthquake (Seismites): Examples from Lake Van Deposits (Turkey)*.
- Woodcock, N.H. 1979. The use of slump structures as palaeoslope orientation estimators. *Sedimentology*, **26**, 83–99.
- ZAMG. 1998. *Seismische Beobachtungen 1998*. Tech. rept.
- ZAMG. 1999. *Seismische Beobachtungen 1999*. Tech. rept.
- ZAMG. 2000. *Seismische Beobachtungen 2000*. Tech. rept.
- ZAMG. 2001. *Seismische Beobachtungen 2001*. Tech. rept.
- ZAMG. 2002. *Seismische Beobachtungen 2002*. Tech. rept.
- ZAMG. 2003. *Seismische Beobachtungen 2003*. Tech. rept.
- ZAMG. 2004. *Seismische Beobachtungen 2004*. Tech. rept.
- ZAMG. 2005. *Seismische Beobachtungen 2005*. Tech. rept.
- ZAMG. 2006. *Seismische Beobachtungen 2006*. Tech. rept.
- ZAMG. 2007. *Seismische Beobachtungen 2007*. Tech. rept.
- ZAMG. 2008. *Seismische Beobachtungen 2008*. Tech. rept.

-
- ZAMG. 2009. *Seismische Beobachtungen 2009*. Tech. rept.
- ZAMG. 2010. *Seismische Beobachtungen 2010*. Tech. rept. 481.
- ZAMG. 2011. *Seismische Beobachtungen 2011*. Tech. rept.
- ZAMG. 2012. *Seismische Beobachtungen 2012*. Tech. rept.
- ZAMG. 2013. *Seismische Beobachtungen 2013*. Tech. rept.
- Zolitschka, B. 2007. Varved Lake Sediments. 3105–3114.

APPENDIX

APPENDIX

MATLAB CODES

27.01.15 16:04 C:\U...\Histogram BestFit HI_09b_2013_6.m 1 of 2

```
clear
close all
clc

% Resolution at which line was exported (e.g. for Drawing precision 1:100000 use ✓
res=1e5)
res = 1e5;

% Length of scale (in mm)
scale = 5;

% Layer thickness (in mm)
T=0.4;

% Load data
C = load(['C:\Users\Tanja\Desktop\Martina\Matlab_Fault_Analysis\HI_09b_2013_scale. ✓
txt']);

C = C/res;
C(:,2) = -C(:,2);

% Compute scale factor for one mm
one_mm = sqrt( (C(1,1)-C(2,1))^2 + (C(1,2)-C(2,2))^2 )/scale;

% Coordinates of scale
xs = C(:,1)/one_mm;
ys = C(:,2)/one_mm;

% Load line and scale
F = load('C:\Users\Tanja\Desktop\Martina\Matlab_Fault_Analysis\HI_09b_2013_6.txt');
F = F/res/one_mm;

% x and y position of line
x = F(:,1);
y = -F(:,2);

% Fault centre position
X = 0.5*(x(3:2:end-1)+x(2:2:end-2));
Y = 0.5*(y(3:2:end-1)+y(2:2:end-2));

% Spacing
S = (X(2:end)-X(1:end-1))./T;

% Number of data
N = length(S);

% CV of spacing
Scv = std(S)/mean(S);

%%%%%%%%%%%%%%%%%%%%%%%%%%%%%%%%%%%%%%%%%%%%%%%%%%%%%%%%%%%%%%%%%%%%%%%%
% Plot histogram with predefined bins
bins = 0:0.25:12;
bin_width = bins(2)-bins(1); % width of bins
n_bins = histc(S,bins); % get counts for each bin
```


27.01.15 16:04 C:\U...\Histogram BestFit HI 09b 2013 6.m 2 of 2

```

area = N * bin_width; % total area of bars
bar(bins+0.5*bin_width,n_bins,1,'FaceColor',.5*[1 1 1]);hold on % plot histogram

% Best-fit distributions
s = linspace(0,40,2000); % generate x-values for theoretical distribution

% Fit best-fit normal distribution
pdnormal = fitdist(S,'normal');
ynormal = area * pdf(pdnormal,s);

% Fit best-fit log-normal distribution
pdlognormal = fitdist(S,'lognormal');
ylognormal = area * pdf(pdlognormal,s);

% Fit best-fit Weibull distribution
pdweib = fitdist(S,'weibull');
yweib = area * pdf(pdweib,s);

% Plot best-fit distributions and add legend
%h(1)=plot(s,ynormal,'r-');
plot(s,ylognormal,'k-');
%h(3)=plot(s,yweib,'b-');
%legend(h,'normal','log-normal','Weibull')
title(['CV = ',num2str(Scv)])
% Make the plot nicer
xlabel('boudin aspect ratio')
ylabel('frequency')
set(gca,'TickDir','out','XTick',0:0.5:5,'XLim',[0 4],'YTick',0:1:20,'YLim',[0 18])
box off
set(gcf,'Color','w')

%%%%%%%%%%%%%%%%%%%%%%%%%%%%%%%%%%%%%%%%%%%%%%%%%%%%%%%%%%%%%%%%%%%%%%%%
min=min(S) %min aspect ratio
max=max(S) %max aspect ratio

```

27.01.15 16:52 C:\Users\Tanja\Desktop...\HI_09b_2013_6.m 1 of 3

```

clear
close all
clc

% Resolution at which line was exported (e.g. for Drawing precision 1:100000 use ✓
res=1e5)
res = 1e5;

% Length of scale (in mm)
scale = 5;

% Load scale
C = load('HI_09b_2013_scale.txt');
C = C/res;
C(:,2) = -C(:,2);

% Compute scale factor for one mm
one_mm = sqrt( (C(1,1)-C(2,1))^2 + (C(1,2)-C(2,2))^2 )/scale;

% Coordinates of scale
xs = C(:,1)/one_mm;
ys = C(:,2)/one_mm;

% Load line and scale
F = load(['HI_09b_2013_6.txt']);
F = F/res/one_mm;

% x and y position of line
x = F(:,1);
y = -F(:,2);

% Fault centre position
X = 0.5*(x(3:2:end-1)+x(2:2:end-2));
Y = 0.5*(y(3:2:end-1)+y(2:2:end-2));

% Spacing
S = X(2:end)-X(1:end-1);

% Throw
T = y(3:2:end-1)-y(2:2:end-2);

% Heave
H = x(3:2:end-1)-x(2:2:end-2);

% Throw polarity
polarity = sum(T)/sum(abs(T));

% CV of spacing
Scv = std(S)/mean(S);

%%%%%%%%%%%%%%%%%%%%%%%%%%%%%%%%%%%%%%%%%%%%%%%%%%%%%%%%%%%%%%%%%%%%%%%%
% Plot of line and scale (for checking)
figure
hold on
plot(x,y,'b-')

```

27.01.15 16:52 C:\Users\Tanja\Desktop...\HI 09b 2013 6.m 2 of 3

```

for i=1:length(X)
    text(X(i),Y(i),[num2str(T(i)), ' / ', num2str(H
(i))], 'HorizontalAlignment','center')
end
plot(xs,ys,'k-','LineWidth',1)
axis equal, box on
xlabel('x (mm)')
ylabel('y (mm)')
title(['Fault system polarity = ',num2str(polarity)])
set(gca,'TickDir','out')
set(gcf,'Color','w')

%%%%%%%%%%%%%%%%%%%%%%%%%%%%%%%%%%%%%%%%%%%%%%%%%%%%%%%%%%%%%%%%%%%%%%%%
% Cumulative number plot
figure
subplot(1,2,1)
plot(flipud(sort(abs(T))),1:length(T),'ko-','MarkerFaceColor','k')
xlabel('throw (mm)')
ylabel('cumulative number of faults')
set(gca,'TickDir','out','YLim',[1 length(T)])
title('Linear x-scale')

subplot(1,2,2)
plot(flipud(sort(abs(T))),1:length(T),'ko-','MarkerFaceColor','k')
xlabel('throw (mm)')
ylabel('cumulative number of faults')
set(gca,'TickDir','out','YLim',[1 length(T)], 'XScale','Log')
title('Logarithmic x-scale')

set(gcf,'Color','w')

%%%%%%%%%%%%%%%%%%%%%%%%%%%%%%%%%%%%%%%%%%%%%%%%%%%%%%%%%%%%%%%%%%%%%%%%
% Staircase plots
xx = zeros(length(X)*2,1);
xx(1:2:end-1) = X;
xx(2:2:end) = X;
xx = [min(x); xx; max(x)];

HH = zeros(length(X)*2,1);
cumH = cumsum(H);
HH(1:2:end-1) = [0; cumH(1:end-1)];
HH(2:2:end) = cumH;

HH = [0; HH; HH(end)];

figure
plot(xx,HH,'b-','LineWidth',1)
xlabel('x-distance (mm)')
ylabel('cumulative heave (mm)')
title(['Total extension = ',num2str(cumH(end)), ' mm'])
set(gca,'TickDir','out')
set(gcf,'Color','w')

%%%%%%%%%%%%%%%%%%%%%%%%%%%%%%%%%%%%%%%%%%%%%%%%%%%%%%%%%%%%%%%%%%%%%%%%
% Cumulative frequency plot of spacing

```

27.01.15 16:52 C:\Users\Tanja\Desktop...\HI 09b 2013 6.m 3 of 3

```
figure
hold on
plot(sort(S), (1:length(S))/length(S), 'ko-', 'MarkerFaceColor', 'k')

xdis = linspace(0,max(S),100);
% Normal distribution
ynorm = normcdf(xdis,mean(S),std(S));
h(1)=plot(xdis,ynorm, 'b-', 'LineWidth',1);

% Lognormal distribution
ylognorm = logncdf(xdis,mean(log(S)),std(log(S)));
h(2)=plot(xdis,ylognorm, 'r-', 'LineWidth',1);

legend(h, 'Normal Distribution', 'Log-Normal Distribution', 'Location', 'SE')
title(['CV = ', num2str(Scv)])
xlabel('spacing (mm)')
ylabel('cumulative frequency')
box on
set(gca, 'TickDir', 'out')
set(gcf, 'Color', 'w')
%%%%%%%%%%%%%%%%%%%%%%%%%%%%%%%%%%%%%%%%%%%%%%%%%%%%%%%%%%%%%%%%%%%%%%%%%%%%%%
%Plot Histogramm

figure
hold on

% Distribution fit

nbins = 10;
histfit(S,nbins, 'lognormal');
h = get(gca, 'Children');

set(h(1), 'Color', 'k')
set(h(2), 'FaceColor', [.5 .5 .5]); % Set properties of bars

legend(h(1), ' Log-Normal distribution fit', 'Location', 'NE')
set(gca, 'TickDir', 'out')
title(['CV = ', num2str(Scv)])
xlabel('Length (mm)')
ylabel('Frequency')
set(gcf, 'Color', 'w')
%box on

%%%%%%%%%%%%%%%%%%%%%%%%%%%%%%%%%%%%%%%%%%%%%%%%%%%%%%%%%%%%%%%%%%%%%%%%%%%%%%
d=size(S) %amount of measurements
min=min(S) %min length of boudins
max=max(S) %max length of boudins
av=mean(S) % average length of boudins
```


HEAVY MINERAL ANALYSIS

Mineral	HI 2	[%]	HI 2 Kontrolle	[%]	HI 2 Kontrolle	[%]	HI 3	[%]	HI 3 Kontrolle	[%]
Epidote		40	38,83	5	25	5	20	45	43,69	3
Zoesite		26	25,24	5	25	11	44	16	15,53	8
Chloritoide		7	6,80			2	8	6	5,83	1
Apatite		10	9,71	2	10	2	8	1	0,97	
Zircon		10	9,71	2	10	4	16	10	9,71	9
Rutile		2	1,94					6	5,83	2
Hornblende		1	0,97	2	10	1	4	4	3,88	
Tourmaline		2	1,94	3	15			6	5,83	
Granet		3	2,91	1	5			2	1,94	1
Kyanite		2	1,94					7	6,80	1
Staurolite										4
Sum	103		100	20	100	25	100	103	100	25
										100
Mineral	HI 4 (1)	[%]	HI 4 (1) Kontr	[%]	HI 4 (2)	[%]	HI 4 (2) Kontr	[%]	Mean	
Epidote	43	39,81	7	26,92	42	40,38	6	24	40,6809255	
Zoesite	21	19,44	8	30,77	24	23,08	11	44	20,8245166	
Chloritoide	4	3,70	3	11,54	5	4,81	1	4	5,28318881	
Apatite					2	1,92	1	4	3,15067214	
Zircon	12	11,11	4	15,38	8	7,69	3	12	9,55522363	
Rutile	6	5,56			2	1,92	1	4	3,81140569	
Hornblende	2	1,85							1,6765552	
Tourmaline	3	2,78	3	11,54	6	5,77			4,07849971	
Granet	12	11,11			12	11,54	1	4	6,8759854	
Kyanite	4	3,70			3	2,88	1	4	3,83154579	
Staurolite	1	0,93	1	3,85					0,23148148	
Sum	108	100	26	100	104	100	25	100		100

Martina Lan Salomon

Personal data:

Date and place of birth: 11 October 1990, Vienna, Austria

Nationality: Austrian

Education:

since 2012:	Master of Science: Geoscience, University of Vienna, Austria Thesis: Seismogenic triggered soft sediment deformation (Hirlatzhöhle, Austria) Supervisor: Dr. Prof. Bernhard Grasemann
2009-2012:	Bachelor of Science: Geoscience, University of Vienna, Austria Thesis: Hydrocarbons in the Vienna Basin, Geological frame-work during an internship at the OMV
2009-2010:	Sinology, University of Vienna, Austria
2005-2009:	BORG Mistelbach, Austria (secondary education) focus on musical & instrumental education

Work Experience

06/2014	Teaching assistant for undergraduate practical course in fossilisation (University of Vienna) Teaching assistant for undergraduate geological mapping course (University of Vienna)
10/2013-02/2014	Teaching assistant for graduate course in microtectonics (University of Vienna) Teaching assistant for undergraduate course in introduction to geology (Vienna University of Technology)
09/2013	Internship: Department of Base and Raw Materials - Division of Mining and Energy - Austrian Federal Ministry of Science, Research and Economy
06/2013	Teaching assistant for undergraduate practical course in fossilisation (University of Vienna) Teaching assistant for undergraduate geological mapping course (University of Vienna)
07/2012	Internship : OMV Exploration & Production; Department: Environment & Waste Disposal
06/2012	Teaching assistant for undergraduate practical course in structural geology and tectonics (University of Vienna)

Relevant skills

Geological mapping	5 weeks course based: B.Sc and M.Sc level (Nassfeld 2014, Stubaital 2013, Ötztal 2013, Schobergruppe 2012, Schönfeld 2011)
Methods	XRD, transmitted and reflected light microscopy
Software	ArcGIS (course based), GOCad (course based), Corel DRAW, MS-Office, Tectonics FP, Petrel (course based), Mathematica (course based), MatLab (course based)
Languages	German (native), English (fluent), Chinese (intermediate), French (beginner), Spanish (beginner)

CV- Martina Lan Salomon

Additional Information

09/2014	PANGEO Austria, Graz (Oral Presentation)
04/2014	European Geosciences Union (EGU) General Assembly, Vienna, Austria (Poster)
10/2012-09/2013	Performance Scholarship University of Vienna
08/2012	maintenance and repairing of hiking trails in the Austrian Alps, Umweltbaustelle OEAV (Austrian Alpine Club)
08/2011	maintenance of alpine pasture areas and highmoors, Umweltbaustelle OEAV (Austrian Alpine Club)

Personal Interests

mountaineering, backcountry skiing, climbing, biking, travelling, cooking and eating